Volume 36
DOE/DP40200-79

LLE Review

Quarterly Report

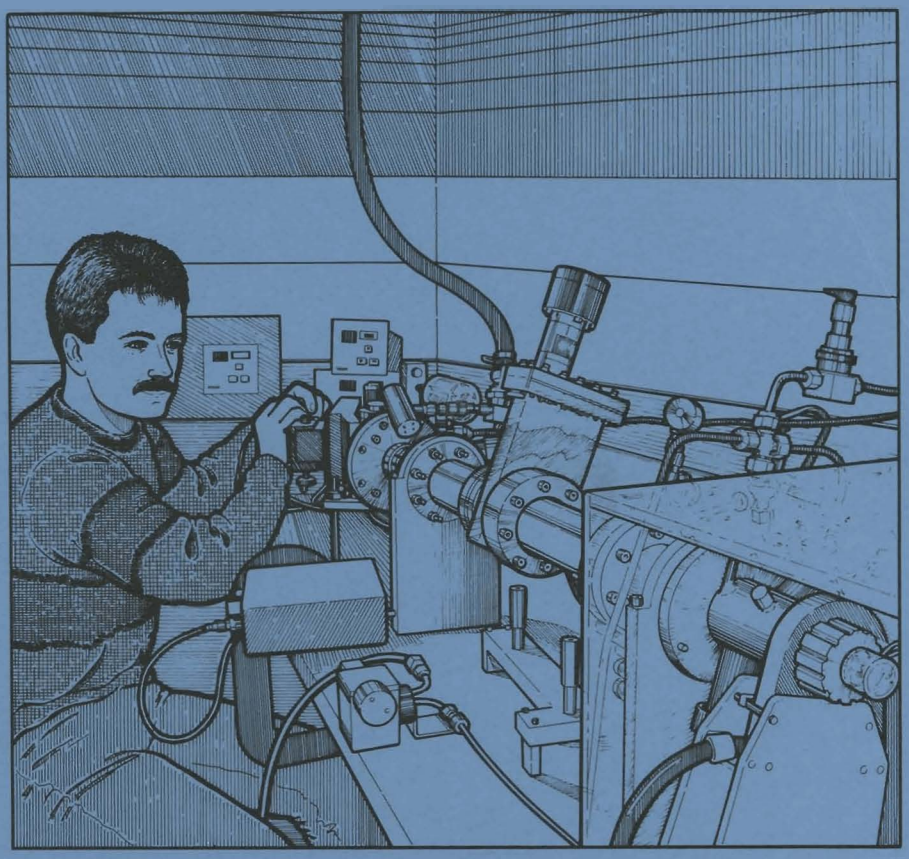

July–September 1988

Laboratory for Laser Energetics
College of Engineering and Applied Science
University of Rochester
250 East River Road
Rochester, New York 14623-1299

Volume 36
DOE/DP40200-79

LLE Review

Quarterly Report

Editor: R. Kremens
(716) 275-4548

July–September 1988

Laboratory for Laser Energetics
College of Engineering and Applied Science
University of Rochester
250 East River Road
Rochester, New York 14623-1299

IN BRIEF

This volume of the LLE Review, covering the period July–September 1988, contains several articles on important diagnostics used during a recent high-density target experiment series; a report on a novel technique for improving laser illumination uniformity on laser-fusion experiments; and a report on nonlocal electron transport simulations as applied to laser-produced plasmas. The advanced technology section has an article discussing multiphoton ionization using the T^3 (table-top-terrawatt) laser system; and a discussion of a new computer code to model x-ray refraction in line-focus geometry. Finally, the activities of the National Laser Users Facility and the GDL and OMEGA laser facilities are summarized.

The following are highlights of the research reports contained in this issue:

- DT (deuterium-tritium) fuel density was measured using the knock-on technique in high-compression experiments. Since the fuel density in these targets significantly moderated the scattered fuel particles, a new technique of analysis and recording of the knock-on fuel particles had to be developed. Analysis of recent experimental results, with measured densities of 100 to 200 times the liquid density of DT, is presented.
- A new system for semiautomated analysis of knock-on data is described. This system, employing a computer, high-power computer-interfaced microscope, and image analysis system,

significantly improves the accuracy and reduces the time necessary for analysis of knock-on track data.

- Neutron diagnostics employed on recent gas and cryogenic target experiments are discussed. Attention to calibration, cross checking, and multiple measurements assure high accuracy. A new system using large scintillators for measurement of secondary neutron yield is outlined.
- A new technique for smoothing laser irradiation on target has been invented. The technique – smoothing by spectral dispersion (SSD) – allows the use of broad bandwidth in frequency-tripled laser systems.
- A fluid-modeling code (SPARK) designed to solve the electron Fokker-Planck equation in two dimensions (2-D) is introduced. The code has shown that in 2-D, thermal smoothing becomes less effective as a result of nonlocal nature of electron transport. This might have important implications in estimation of ablation pressure uniformity.
- Multiphoton ionization in noble gases is being studied, using the highest intensities available at a wavelength of 1.053 μm. Ne^{6+}, Ar^{8+}, Kr^{8+}, and Xe^{12+} have been observed using a time-of-flight ion spectrometer. Using the T^3 laser system, intensities of up to 10^{17} W/cm^2 have been generated in picosecond pulses for this experiment.

CONTENTS

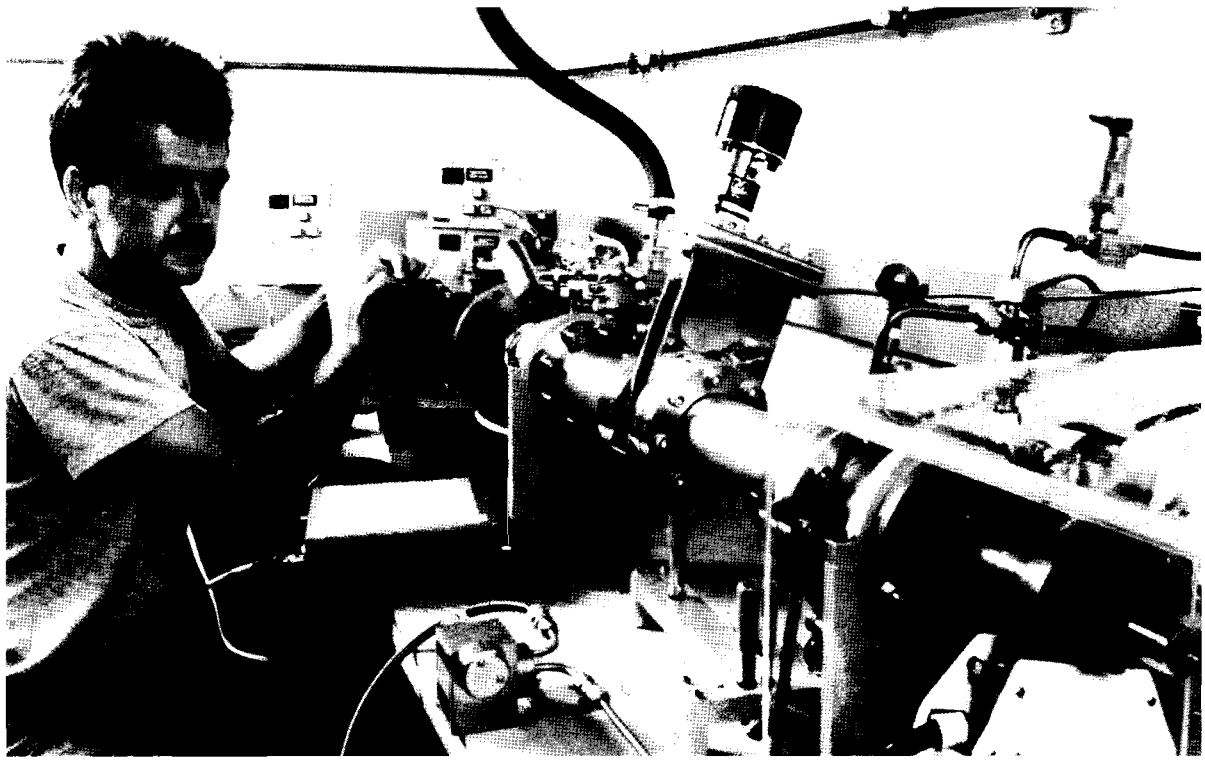

David Bradley, a scientist in the OMEGA Experimental Group, is shown testing the microchannel-plate-intensified grating spectrograph (McPIGS) using a sliding spark plasma discharge source. The source, which emits line radiation extending from ~ 50 Å through to the visible, is used for calibrating a number of UV and soft x-ray diagnostics.

Section 1
PROGRESS IN LASER FUSION

1.A Diagnosing High Density with "Knock-Ons"

The DT fuel density in recent high-compression experiments[1,2] at LLE was measured using the "knock-on" diagnostic.[3] Previously this diagnostic had been used only in low-density experiments in which there was a negligible amount of slowing down of the knock-on particles within the target.[4,5] In the present experiments, the target density-radius product (ρR) was sufficiently large to significantly moderate the knock-on particles, so that a new technique had to be developed to accommodate the distorted spectrum.

The principle behind the knock-on diagnostic is as follows (see Fig. 36.1). DT fusion reactions in the fuel produce energetic (14-MeV) neutrons. As the neutrons traverse the fuel region, there is a small probability that they will elastically scatter off of deuterium (D) and tritium (T) ions in the fuel. The number of such scattering events is directly proportional to the fuel ρR times the neutron yield Y. Thus, by counting the number of elastically scattered D and T ions (knock-ons) and by measuring the neutron yield, it is possible to infer the fuel ρR. The knock-ons were detected in the solid-state track detector CR-39. The technique used to discriminate between D or T knock-on tracks and tracks produced by other charged particles restricted the counted tracks to only a fraction F ($\lesssim 10\%$) of the total number of knock-ons. Only those tracks that crossed the entire CR-39 thickness with entrance diameters larger than a specified number were counted, corresponding to knock-ons in a well-defined energy window. (See Ref. 1 for a discussion of this selection technique.) As a result, the relation

between fuel ρR and measured quantities depends on the fraction F:

$$\rho E_{\text{fuel}} = \frac{Q}{YF} \times 5.4 \times 10^3 \text{ mg/cm}^2 , \quad (1)$$

where Q is the number of tracks that meet the selection criterion. The constant factor is $(M_D + M_T)/(\sigma_D + \sigma_T)$, where σ_D and σ_T are the elastic scattering cross sections for 14-MeV neutrons on deuterons and tritons (0.62b and 0.92b, respectively), M_D and M_T are the respective masses, and equimolar DT is assumed.

Proper implementation of the diagnostic requires determining the fraction F of those knock-ons that are in the selection energy window. Unfortunately, F is a function of target conditions. If the knock-ons are slowed down within the target, a different part of the spectrum will move into the track-detector energy window, resulting in a different value for F. In general, F is a function of both fuel and shell ρR, as well as temperature, so that the ratio Q/Y will not uniquely determine the fuel ρR.

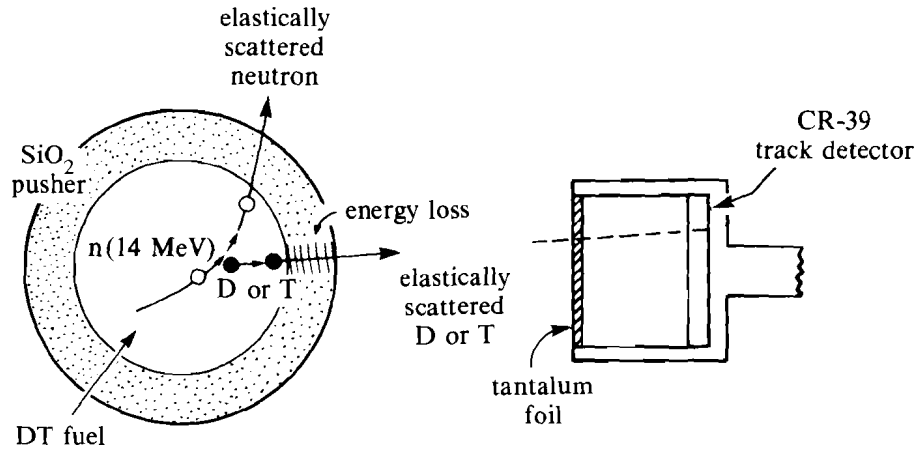

Fig. 36.1
Schematic of the knock-on diagnostic.

An example of how F can change with target conditions is illustrated in Fig. 36.2, showing the superposition of the deuteron and triton knock-on spectra. (It is not necessary to discriminate between these particles.) The shape of the spectrum, with peaks at high and low energy, results from the asymmetric cross section for 14-MeV neutron elastic scattering, which is peaked for forward and backward scattering in the center of mass system. In this example, a 40-μm tantalum filter was used to bring the triton peak into the energy window of the track

detector when there is no significant slowing down of the knock-ons in the target [Fig. 36.2(a)]. For conditions where there is increased slowing down due to, for instance, increased ρR or decreased temperature, the triton peak will shift out of the energy window to lower energies; also, the fraction of the total spectrum that is detected will be reduced, as in Figs. 36.2(b) and 36.2(c).

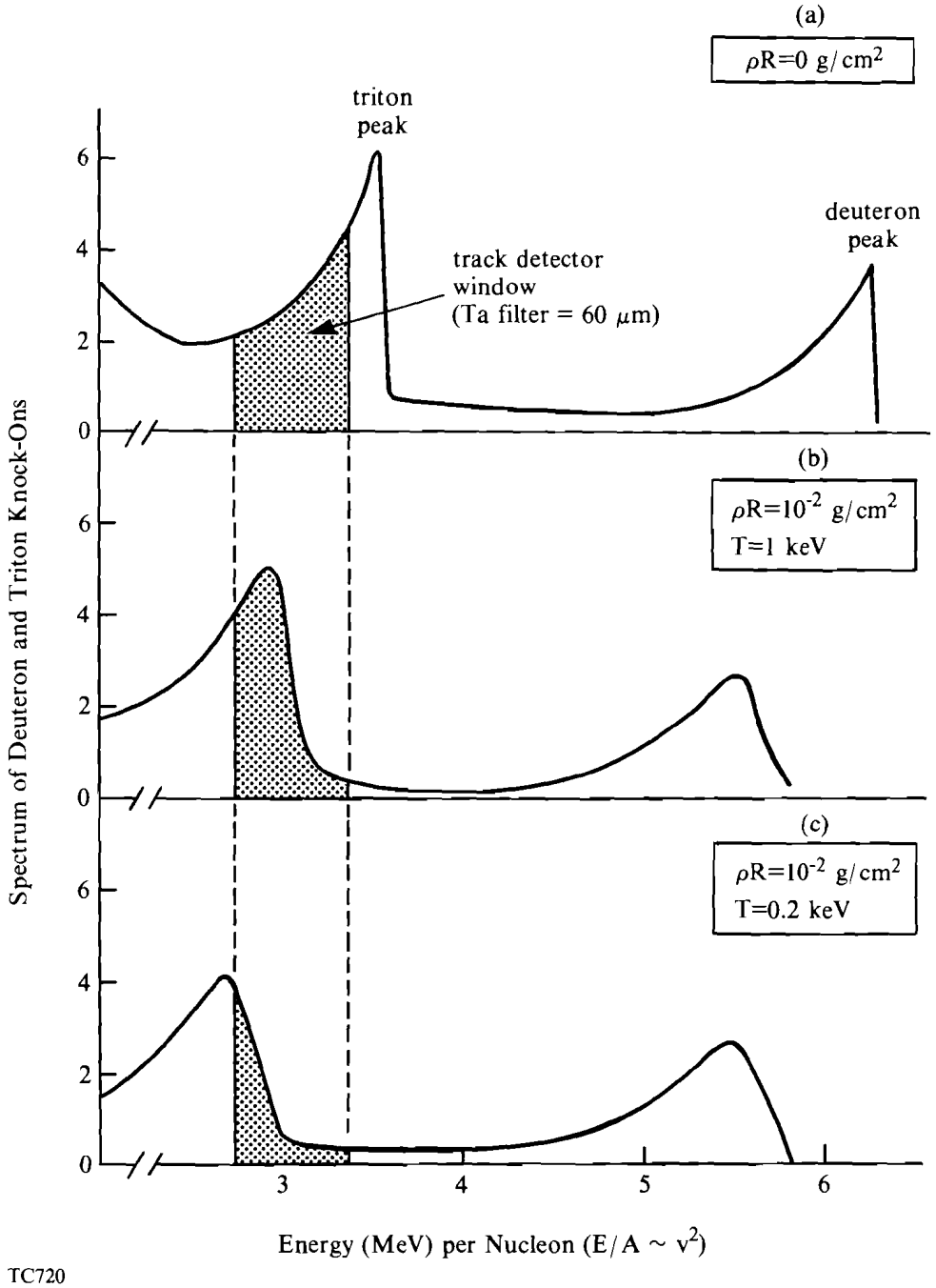

Fig. 36.2
Example showing how target conditions affect the fraction F of knock-ons in the track-detector energy window.

To resolve this difficulty, we have replaced the single-foil track detector with multiple, stacked foils in two configurations, allowing us to measure a larger fraction of the knock-on spectrum and to remove the sensitivity of F to target conditions for the range of ρR attained in the OMEGA experiments. With this technique, F becomes a single number ($0.85 \pm 5\%$) over the range of total target ρR varying from 0 to ~ 50 mg/cm^2, with the track count Q in Eq. (1) now replaced by the sum of tracks meeting the selection criterion in each of four track-detector foils. For total target ρR greater than ~ 50 mg/cm^2, F again becomes dependent on target conditions, but it will always remain less than ~ 0.085 so that, at worst, use of $F = 0.085$ in Eq. (1) will yield a lower bound for the fuel ρR. This result is model independent and does not depend on the source of knock-on spectral distortion within the target, whether it is from the fuel ρR, the shell $\rho \Delta R$, temperature, or temporal or spatial variation of conditions in the target.

The five-foil, two-stack configuration of CR-39 used in the experiments is shown in Fig. 36.3. The first tantalum filter is required to block target debris and charged particles produced in the DD and DT nuclear reactions. The stacked CR-39 foils serve a dual purpose. Each detector is used (1) to detect knock-on tracks and (2) to slow down knock-on particles so that a different part of the spectrum is in the selection energy window of subsequent track detectors. The tantalum foils also help shift the knock-on spectrum. The most energetic of the knock-on particles leave tracks in the farthest foil. The first CR-39 foil in each of the two stacks detects the same part of the spectrum and is used for consistency checks. Although no attempt was made to separate deuterons from tritons, the first foil predominantly detected the tritons while the deuterons were distributed among the remaining four detectors.

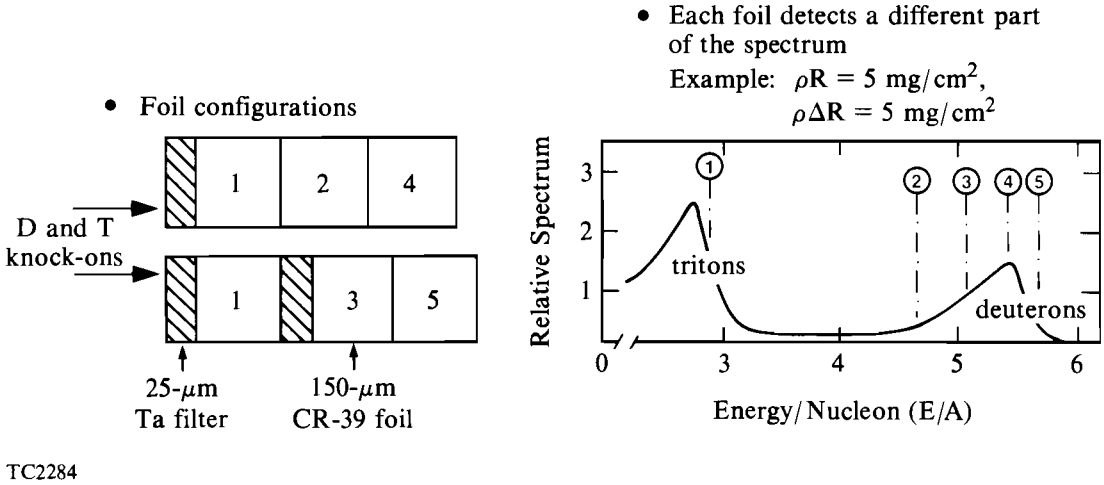

Fig. 36.3
The five-foil set used in the high-density experiments and the approximate region of the knock-on spectrum that meets the selection criterion for each foil.

The effect of knock-on moderation within the target is shown in Fig. 36.4 for the five-foil system, based on computer simulations of two targets with total ρR = 20 mg/cm^2 and 40 mg/cm^2. The slow-down of the knock-ons is clearly discernible with the increased ρR, as the deuteron peak moves from foil 5 to foil 3, and the triton peak moves partially out of the window of foil 1. Clearly, the fraction of the knock-on spectrum in the window of any single detector has changed substantially due to the spectrum moderation. However, note that the sum of tracks in foils 2-5 remains relatively constant, ~8.5%, as it represents the total fraction of knock-ons in the high-energy deuteron peak and does not depend on the exact position of the peak. Furthermore, it does not depend on what conditions in the target produced the moderation of the spectrum. Only after the total ρR exceeds about 50 mg/cm^2 will the moderation be large enough to start shifting the peak out of these foils, in which case, the sum of tracks will be less than 8.5%. Thus, F = 8.5% represents an upper bound for this parameter in Eq. (1). It provides for an accurate determination of fuel ρR for total target ρR less than ~50 mg/cm^2; otherwise, it provides a lower bound on the fuel ρR.

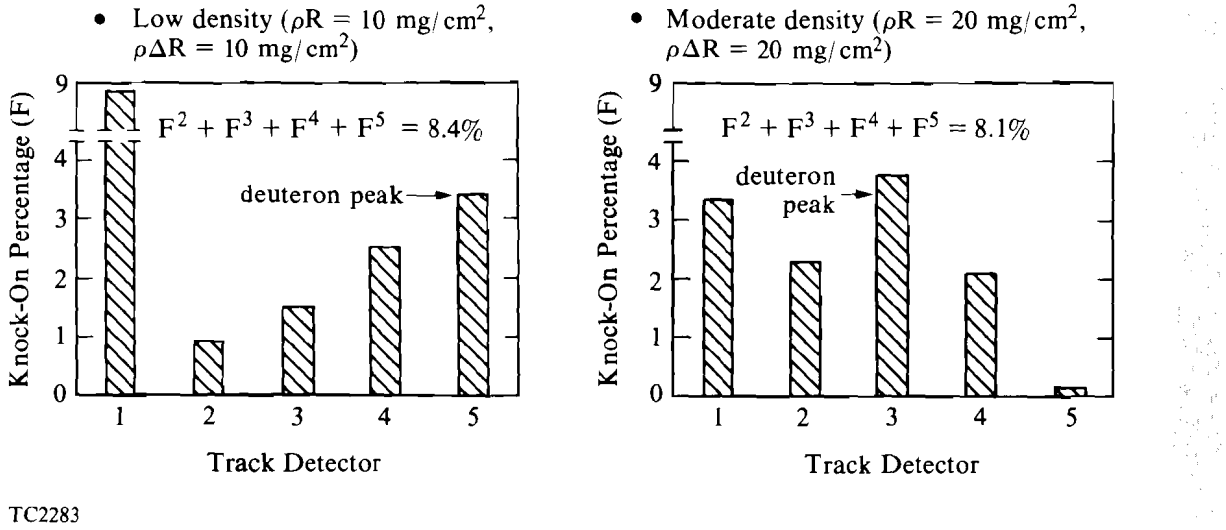

Fig. 36.4
Relative number of knock-ons in each of the five CR-39 foils for the two cases of total target ρR equals 20 mg/cm^2 and 40 mg/cm^2.

Figures 36.5 and 36.6 illustrate application of this diagnostic to experimental data. Whereas the diagnostic itself is model independent, it is useful to deploy a particular model to demonstrate at what point the diagnostic becomes sensitive to target conditions. The model assumes a sphere of constant-density DT fuel surrounded by a constant-density glass shell. For the following examples, the results are relatively insensitive to the temperatures or densities of the fuel and shell, or to the distribution of neutron production in the fuel. The

values of fuel ρR and shell $\rho \Delta R$ were varied and the resulting moderated knock-on spectrum and track-detector response were calculated.

Figure 36.5 shows an example of a moderate-density gaseous DT experiment. The curve marked "deuterons" shows the region of fuel $\rho \Delta R$ that would be consistent with the number of knock-on tracks observed in foils 2–5 for that particular shot. The width of the curve is determined by the statistical error, given by the square root of the number of counts. Note that the curve rises nearly vertically, uniquely determining the fuel ρR, and is relatively independent of $\rho \Delta R$. The curve marked "tritons" is determined by the number of tracks in foil 1, which is dominated by the triton high-energy peak. This curve initially rises vertically, but then shifts to the right as the increasing target ρR slows the tritons out of the energy window of this detector, i.e., with a decrease in the fraction of knock-ons Q, the observed number of tracks can only be produced by a larger value of fuel ρR. Thus, the triton curve alone cannot uniquely determine the fuel ρR. However, the intersection of the triton and deuteron curves shows a point of ρR and $\rho \Delta R$ that is consistent with both track observations. Whereas this diagnostic was designed to determine only fuel ρR, we now also find that $\rho \Delta R$ can be determined (though the latter is somewhat model dependent) by demanding consistency among all the track-detector foils.

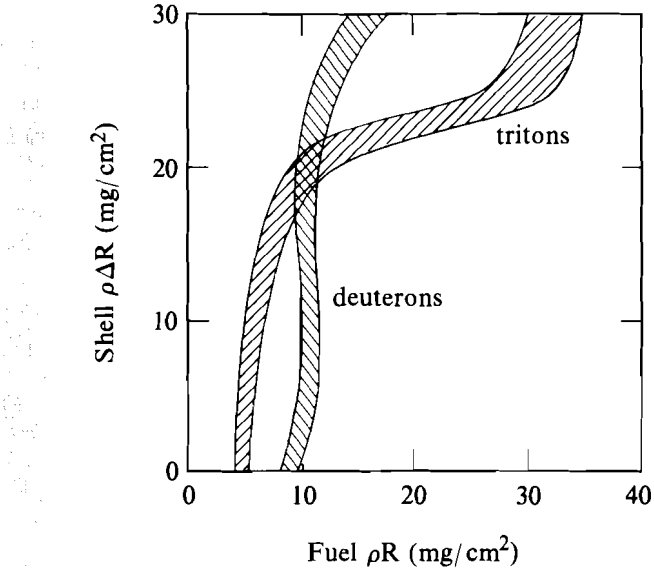

Shot: 15975D
Yield: 4×10^8
Tracks:
D = 128
T = 67
$\Delta\Omega/4\pi = 2 \times 10^{-3}$
Target:
P = 30 atm
R = 137 μm
ΔR = {3 μm (SiO^2), 4 μm (CH)}

Fig. 36.5
Region of fuel ρR and shell $\rho \Delta R$ consistent with the number of tracks observed in a moderate density implosion with gaseous DT. The "deuteron" curve represents the sum of tracks in foils 2–5 meeting the selection criterion. The "triton" curve represents the tracks in foil 1.

The second example (Fig. 36.6) is for a shot aimed at higher density, this time using cryogenic DT fuel. For this shot, the higher fuel ρR was not enough to compensate for the low neutron yield, which resulted in a small number of knock-ons. This is reflected in the much wider curves in Fig. 36.6. The deuteron curve now rises nearly vertically only until $\rho\Delta R + \rho R \approx 50$ mg/cm^2; then it moves to the right as the deuteron peak begins to move out of the combined windows of track detectors 2–5. A lower limit on the fuel ρR is well determined at $\sim$25 mg. The kink in the curve for $\rho\Delta R < 5$ mg/cm^2 is due to the presence of some high-energy tritons in foil 2, but these are quickly moved out at higher $\rho\Delta R$ values. The intersection of the deuteron and triton curves suggests a shell $\rho\Delta R$ value of $\sim$20 mg/cm^2, which is consistent with "rad chem" measurements on similar targets.

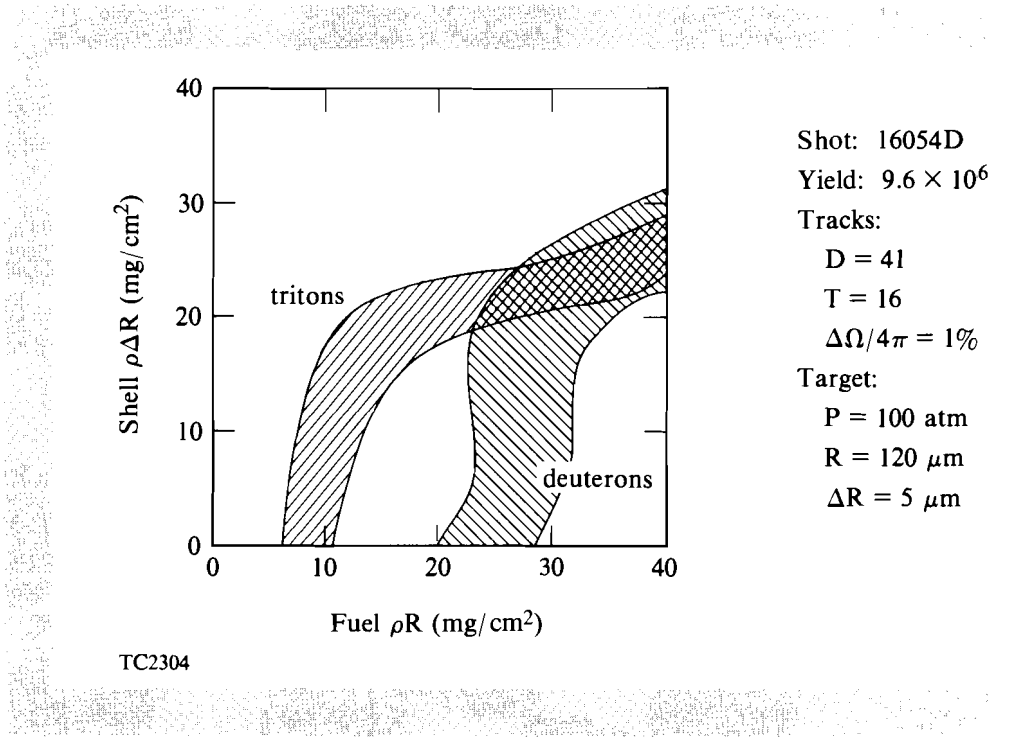

Fig. 36.6
Same as Fig. 36.5, but for a higher-density implosion using cryogenic DT fuel.

In summary, a technique has been developed to measure fuel ρR with knock-on particles in a model-independent way for experiments where the total target ρR is less than $\sim$50 mg/cm^2. The technique takes into consideration moderation of the knock-ons within the target and is independent of the moderation source whether it be in the fuel or shell. Even if there is mixing between the fuel and shell, the diagnostic measures the ρR of the fuel portion. In addition, $\rho\Delta R$ of the shell can be estimated by demanding consistency among the number of tracks in different foils.

ACKNOWLEDGMENT

This work was supported by the U. S. Department of Energy Office of Inertial Fusion under agreement No. DE-FC08-85DP40200 and by the Laser Fusion Feasibility Project at the Laboratory for Laser Energetics, which has the following sponsors: Empire State Electric Energy Research Corporation, New York State Energy Research and Development Authority, Ontario Hydro, and the University of Rochester. Such support does not imply endorsement of the content by any of the above parties.

REFERENCES
1. R. L. McCrory, J. M. Soures, C. P. Verdon, F. J. Marshall, S. A. Letzring, S. Skupsky, T. J. Kessler, R. L. Kremens, J. P. Knauer, H. Kim, J. Delettrez, and R. L. Keck, *Nature* **335**, 225 (1988).
2. F. J. Marshall, S. A. Letzring, C. P. Verdon, S. Skupsky, R. L. Keck, J. P. Knauer, R. L. Kremens, D. K. Bradley, T. Kessler, J. Delettrez, H. Kim, J. M. Soures, and R. L. McCrory, "Cryogenic Laser Fusion Target Implosion Studies Performed with the OMEGA UV Laser System" (submitted for publication).
3. S. Skupsky and S. Kacenjar, *J. Appl. Phys.* **52**, 2608 (1981).
4. S. Kacenjar, S. Skupsky, A. Entenberg, L. Goldman, and M. Richardson, *Phys. Rev. Lett.* **49**, 463 (1982).
5. S. Kacenjar, L. M. Goldman, A. Entenberg, and S. Skupsky, *J. Appl. Phys.* **56**, 2027 (1984).

1.B A Semiautomated Knock-On Recording System

The "knock-on" technique for measuring target density has been described elsewhere in this issue. Here we describe our new semiautomated counting and measuring system, which has considerably eased the task of making the actual measurement.

Knock-ons are detected in thin ($\sim$150-μm) CR-39 plastic. The ions passing through the plastic damage it and, if the plastic is later etched in a hot sodium hydroxide solution, small pits can be observed where the particles entered on the front surface and exited on the back surface.

In order to avoid counting noise pits produced by protons or defects in the plastic, while obtaining energy information on the D and T ions, it is necessary when counting to note the diameter of the pits and if a pit on the top surface is coincident with a pit on the bottom surface (the particle made it all the way through the plastic) or not (it did not make it all the way through). Since the pits are small, 10 to 20 μm in diameter, this counting and measuring must be done under a microscope; because of the resulting limited field of view, many fields must be counted to cover an entire detector. In the past this has been done entirely by hand using a conventional microscope – a very tedious and slow process.

In order to improve the speed and accuracy with which knock-on detectors can be counted, LLE has assembled a computerized microscope system. This system consists of a Nikon optical microscope equipped with both a diascopic (transmitted) and episcopic (reflected) bright-field/dark-field illumination system. The microscope

has been fitted with a Maerhauser computer-controllable stage with 0.25-μm resolution and focus control. The microscope image is fed by a Javelin CCD camera to a Data Translation frame grabber installed in a Digital Equipment VAXstation II/GPX workstation, which also provides stage control. In addition to providing the digitized image to the VAXstation, the frame grabber drives a video monitor to allow direct display of its contents.

At present the system operates in a semiautomatic mode, i.e., an operator is required to recognize a track, and the system handles track measurement, recording, and scan pattern control. Track measurement is quite simple. While viewing the image on the frame grabber monitor, the operator uses the VAXstation mouse to position a cursor on a track and then clicks the mouse. The system measures the track and outlines it, and the operator verifies that the measurement is satisfactory. Should the outline be unsatisfactory, the operator has various image-filtering options as well as microscope illumination options that can enhance the image to allow proper measurement. A re-click on the mouse will then cause the system to remeasure the track. The operator shifts to the other side of the detector with a click on another mouse key. If there is a coincident track, it is measured. The operator then returns to the top of the detector and continues measuring any other tracks in view. Once all tracks in view are measured, the press of a key advances the stage to the next location on the detector.

The system records considerable information about a track. In general, since the particles may go through the detectors at small angles, the tracks are ellipsoidal. Therefore, the system records major and minor track diameter, orientation, and track position for both top and bottom surface in the case of coincident tracks. Track-diameter-measurement repeatability is better than 0.2 μm and position repeatability is better than 1 μm.

In addition to making the measurement process considerably easier, the new system permits us to look at the data in greater detail. For example, we can readily produce histograms of the coincident, noncoincident diameter distribution, which permits a direct determination of the critical track diameter below which protons can no longer be distinguished from deuterons and tritons. We can also compare counts on a track-by-track basis on measurements made by different operators on the same detector, to provide an indication of count accuracy.

Because of the computer-controlled stage and track coordinate recording, we are able to use detector configurations that we could not have considered without the computerized system. In fact, our current configuration, which utilizes circular detectors with annular filtering, would not be countable without such a system.

The system is easily programmable and it can be readily changed to meet changing requirements. An obvious enhancement to the system would be automatic track recognition, which could eliminate the need

for an operator. However, while the eye has no problem distinguishing the rather distinctive appearance of particle tracks from background pits, accomplishing this reliably in software would be a formidable task.

In summary, this system provides a versatile, reasonably fast, and accurate means of making a measurement critical to evaluating ICF target performance.

ACKNOWLEDGMENT

This work was supported by the U. S. Department of Energy Office of Inertial Fusion under agreement No. DE-FC08-85DP40200 and by the Laser Fusion Feasibility Project at the Laboratory for Laser Energetics, which has the following sponsors: Empire State Electric Energy Research Corporation, New York State Energy Research and Development Authority, Ontario Hydro, and the University of Rochester. Such support does not imply endorsement of the content by any of the above parties.

1.C Neutron Diagnostics

Neutron diagnosis of compressed thermonuclear fuel has been an important gauge of target performance since the earliest days of laser-driven inertial confinement fusion. In this article, we will describe the neutron diagnostics used on a recent series of high-density target-implosion experiments to measure neutron yield, shell areal density, fuel areal density, and fuel ion temperature.

Our diagnostic philosophy during this campaign was to make simultaneous measurements of as many parameters as possible, using a variety of cross-checked techniques.

For deuterium-tritium (DT) fuel, we measure neutron yield using an activation technique based on the reaction $^{63}Cu(n,2n)^{62}Cu$. This activation results in decay by electron-positron annihilation, producing two 0.511-MeV gamma rays, which are detected in a standard slow coincidence system. The time intervals during which counting occurs are controlled automatically starting from laser irradiation time (Fig. 36.7). The advantages of the copper activation system include

1. high-energy threshold for the reaction (10.5 MeV) (reduces the effects of scattered neutrons),
2. relatively short half-life (manageable counting time and high decay rate),
3. the availability of a coincident reaction (reduces background), and
4. absolute-detector efficiency calibration using readily available nuclear sources.

In particular, the ability to measure the absolute detection system efficiency allows us to determine the thermonuclear yield of our

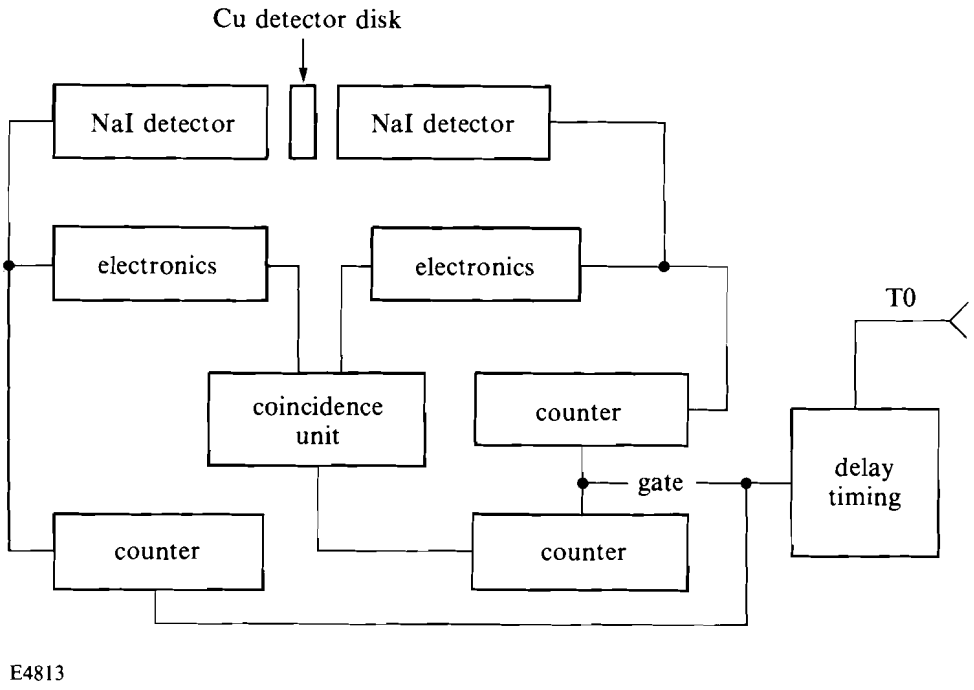

Fig. 36.7
Copper, slow-coincidence system. 'Electronics' consists of a photomultiplier tube preamplifier, amplifier, and timing single-channel analyzer. The detectors are enclosed in a 7.6-cm-thick lead jacket to shield from background radiation.

experiments from only geometric quantities and measured parameters. Thus,

$$Y = c\{\epsilon g\,[1 - e^{(-\sigma n l)}]\}^{-1} \quad ,$$

where Y is the neutron yield of the target; ϵ is the absolute detector efficiency; g is the solid angle subtended by the activation sample; σ is the cross section for the copper reaction; n is number density of copper atoms; l is the thickness of the copper activation sample; and c is the number of detected decays. The sensitivities and range of applicabilities of all our yield measurement systems are listed in Table 36.I.

Table 36.I
Detector positions, sensitivities, and sizes of yield measurement systems.

Detector	Solid Angle (% 4π)	Yield for 30% Error
2 m	0.050	1×10^5
3.5 m	0.016	3×10^5
4 m	0.003	1×10^6
LARD	0.250	1.5×10^4
Copper	0.005	7.8×10^6

E4546

Our second activation detector is a thermalizing detector employing the silver reactions:

$$^{107}\mathrm{Ag}(n, \beta^-)^{108}\mathrm{Ag}$$

and

$$^{109}\mathrm{Ag}(n, \beta^-)^{110}\mathrm{Ag} \ .$$

This device employs a neutron-thermalizing jacket of polyethylene surrounding four Geiger-Muller tubes wrapped with silver foil (Fig. 36.8). The cross sections for these reactions are a strong function of incident neutron energy. This, along with the fact that the neutrons incident on the detector system may be only partially thermalized by the polyethylene jacket, makes first-principle calibration of this detector difficult. Additionally, all thermalizing detectors are susceptible to scattering from diagnostics, experimental chamber, and support structures. However, the method is equally applicable for the measurement of DT or DD fuel primary yield and is our primary-yield diagnostic for pure DD fuel targets. We calibrate the silver detection system *in situ* against the copper activation system for DT fuel. For DD fuel, we calibrate the silver system by counting proton tracks in CR-39 track detector from the reaction branch:

$$^2\mathrm{D} + {}^2\mathrm{D} \rightarrow {}^3\mathrm{T} + p$$

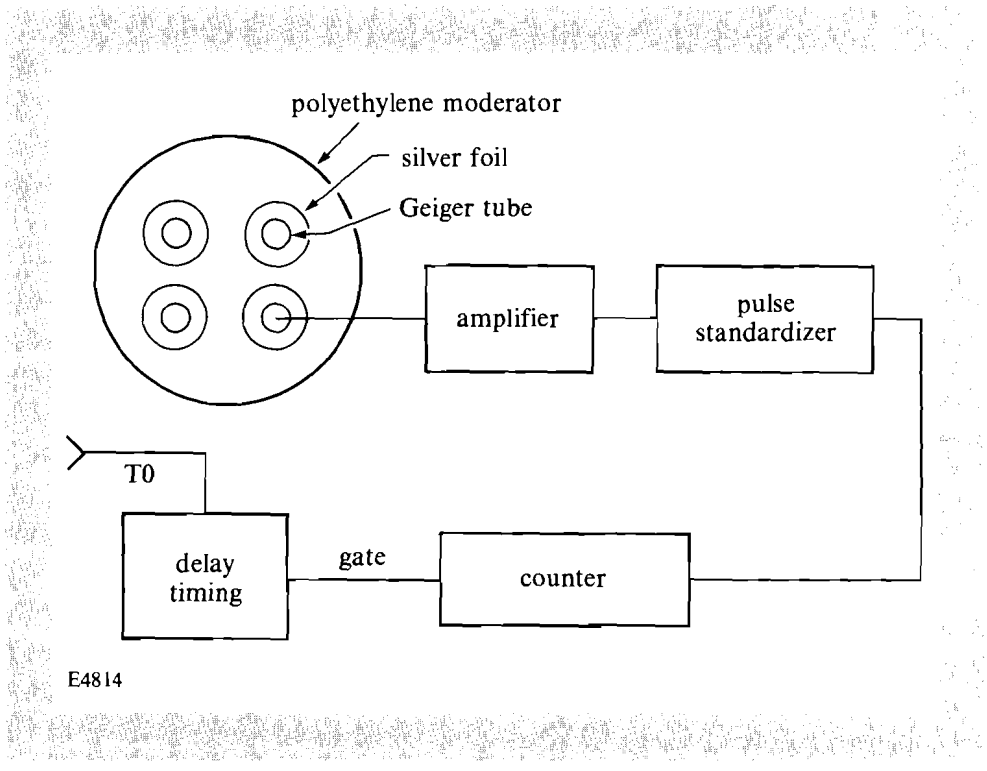

Fig. 36.8
Silver activation detector. The thermalizing jacket of polyethylene is 20 cm in diameter and 30 cm in length.

The number of tracks, along with the known track-detector geometry, measures the absolute yield from this reaction branch, which can be compared to the number of detected decays from the silver activation system to give the detector efficiency. Low-density, high-yield targets are used for these calibrations to reduce the slowing and stopping of 3.02-MeV protons in target and shell material.

A recent addition to the yield-measurement instruments utilizes a large (15-cm-diameter × 15-cm-length) sodium iodide activation detector. The sodium atoms in the detector are activated and "self-detected." This method utilizes the reaction:

$$^{23}\mathrm{Na}(n,\alpha)\ ^{20}F$$

$$^{20}F \rightarrow {}^{20}\mathrm{Ne} + \gamma(1.63\ \mathrm{MeV}) + \beta^{-}\ (5.4\ \mathrm{MeV})\ ,$$

which has a 4-MeV reaction threshold and an 11.4-s half-life. The detectors' large size, proximity to the target (85 cm), and short-activation half-life affords high sensitivity, low background, and simplicity of operation.

The activation-yield measurement systems described above have been integrated into the OMEGA shot summary reporting by using a CAMAC counter interfaced to the DEC PDP-11-based data acquisition system (Fig. 36.9). An IBM-PCAT-type microcomputer is used as a monitor to determine long- and short-term backgrounds and background histories. The microcomputer enables us to maintain an accurate assessment of the adjustment of the activation-detection systems.

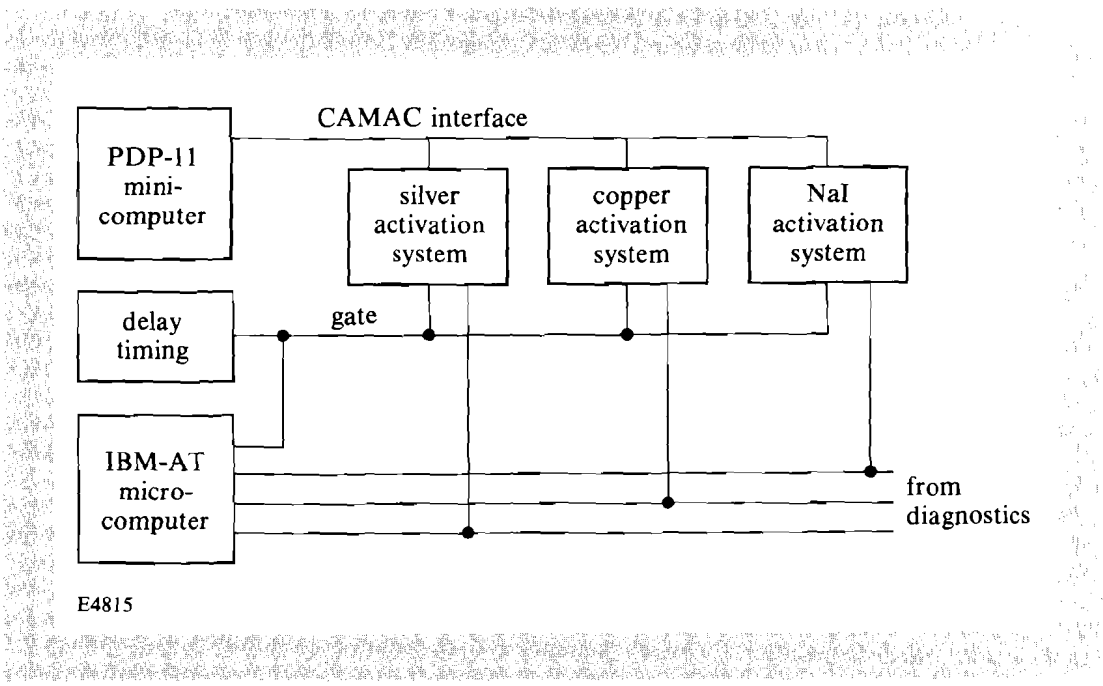

Fig. 36.9
Data collection and recording. The PDP-11 experimental operations minicomputer (CER) collects data from the experiment and generates a data base and a post-shot-data summary sheet. The IBM PC-AT-type microcomputer is equipped with five high-speed counters, recording pulses from the detection systems during background acquisition.

Neutron-averaged shell areal density $<\rho\Delta r>$ is measured using neutron activation of the silicon in the target shells. This technique, employing a highly efficient (35%) beta-gamma coincidence detector and a rapid-extraction, target-debris-collection system, has been described in several recent articles.[1,2] By using special low-activity shielding and carefully adjusting coincidence timing using a time-to-pulse height converter (TPHC), we have been able to reduce the background of this system to 0.3 counts per minute, extending the useful detection threshold to

$$Y <\rho\Delta r> \geq 1.3 \times 10^9 \frac{\text{mg}}{\text{cm}^2} .$$

The IBM-PCAT-type microcomputer mentioned above is also used to record the background history of the shell-density apparatus and monitor the decay rate of activated shell debris during data acquisition (Fig. 36.10).

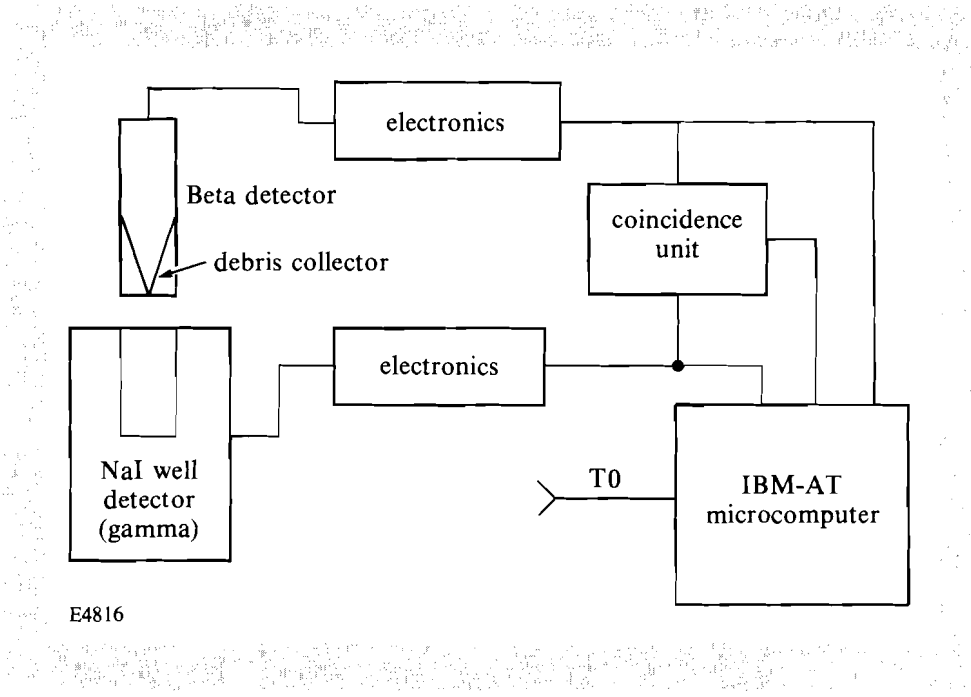

Fig. 36.10
Rad-chem system. The debris collection cone is placed in the beta detector after post-shot rapid extraction from the target chamber. The detectors form a beta-gamma coincidence system. 'Electronics' consists of a photomultiplier tube preamplifier, amplifier, and timing single-channel analyzer. The detectors are housed in 10 cm of low-activity lead, and 0.5 cm of copper to reduce background radiation.

Measurement of the yield of secondary DT fusion neutrons during the implosion of initially pure DD fuel targets has been suggested as a gauge of the fuel areal density.[3-6] Secondary neutrons result from the following reaction chains:

$$^2\text{D} + {}^2\text{D} \rightarrow n \text{ (2.45 MeV) ("primary" neutron)} + {}^3\text{He}$$

$$^2\text{D} + {}^2\text{D} \rightarrow {}^3\text{T} + p$$

$$^2\text{D} + {}^3\text{T} \rightarrow n \text{ (14.01 MeV) ("secondary" neutron)} + {}^4\text{He} .$$

The number of secondary neutrons produced in this reaction depends in a detailed way on the reaction cross sections, fuel density distribution, fuel temperature, and number density. For the simplest case of low-areal-density (< 10 mg/cm^2), high-temperature (10-KeV or more) fuel, it can be shown[4]:

$$<\rho r> = 12.05\, N_{DT}/N_{DD} \text{ g/cm}^2 ,$$

where N_{DT} is the number of secondary neutrons and N_{DD} is the number of primary neutrons. For our target experiments, simulation of secondary/primary neutron ratio is obtained using a post-process job on the one-dimensional computer code *LILAC*.

The secondary measurement system employed during the recent campaign consists of four, large scintillator-photomultiplier assemblies. The detector packages are positioned at 2 m, 3 m, and 3.5 m from the target and provide a useful detection range of almost five orders of magnitude. Each detector is shielded from *n*-gamma scattering radiation by 1.5 cm of lead and is positioned so that the *n*-gamma pulse from the DD primary neutron burst is separated in time from the DT neutron signal by greater than the detector time resolution. This is important for unambiguous identification of detected signals. The smaller detectors (20-cm diameter, 10-cm thick) use Amperex type XP2020 photomultipliers coupled to plastic scintillators in light-tight aluminum housings, while the larger detectors (60-cm diameter, 15-cm thick) use RCA/Burle Industries type-8575 PMT's and liquid scintillator contained in a liquid-tight, reflective-paint-coated housing.

In the hydrogenous scintillating media that are used in our system, detection of neutrons is effected through elastic scattering of scintillator protons by the incident neutrons. The distribution of recoil proton energies depends on the differential scattering cross section as a function of angle. For the case of *n-p* scattering, the scattering is isotropic, giving a box spectrum extending from zero to the maximum neutron energy. Because of the distribution in proton recoil energies, there is not a one-to-one correspondence between observed photomultiplier charge and neutron flux. This results in poorer statistics than would be expected from a conventional pulse-counting system. In the limit of large numbers of detected neutrons or large (total capture, thermalizing) detectors the statistical error associated with this process is small. Our strategy has been to maximize the solid angle and detection efficiency of the scintillator system to reduce this statistical error.[7]

The scintillator system is calibrated on pure DT fuel shots by comparison with the copper activation system. In order to avoid saturating the photomultipliers, calibration shots are done with reduced photomultiplier gain and/or optical filters in front of the photomultipliers. The scintillating medium itself is linear over many decades of light output. This calibration gives the average detected charge per neutron, but does not measure the distribution of detected charge. The width of the current-pulse distribution associated with the recoil protons is measured by irradiating each detector with neutrons from a californium-252 spontaneous fission source and measuring the current-pulse-height distribution using a conventional nuclear counting system. Since the californium source has a broad neutron energy distribution, the width of the current pulse distribution is greater than that obtained with a monoenergetic neutron source. Both the linearity and gain of the each photomultiplier are measured with a pulsed light source.

The fuel-ion temperature for these experiments was measured by time-of-flight neutron spectroscopy. This method, as applied to inertial confinement fusion, was originally described by Brysk.[8] Two detectors are deployed, at 1.8 m and 10 m, for DD and DT neutrons, respectively. These spectrometers consist of a quenched scintillator

(Bicron BC-422, 1% quench) optically coupled to a channel-plate photomultiplier (ITT f4129). The photomultipliers are installed in housings designed to eliminate electrical discontinuities and pulse distortion (Fig. 36.11). The nearly Gaussian output pulse from this detector is shown in Fig. 36.12. The recording system, alignment, and collimation of this detector have been described previously.[1] For the present detector distances and system time resolution, the minimum measurable ion temperatures are

DT fuel (14-MeV neutrons): $T = 0.8$ KeV for $Y > 3 \times 10^8$,

DD fuel (2.45-MeV neutrons): $T = 0.8$ KeV for $Y > 10^7$.

The data from the experiment, consisting of oscillographic recordings on film, is hand digitized and fit to a Gaussian waveform to give the fuel-ion temperature.

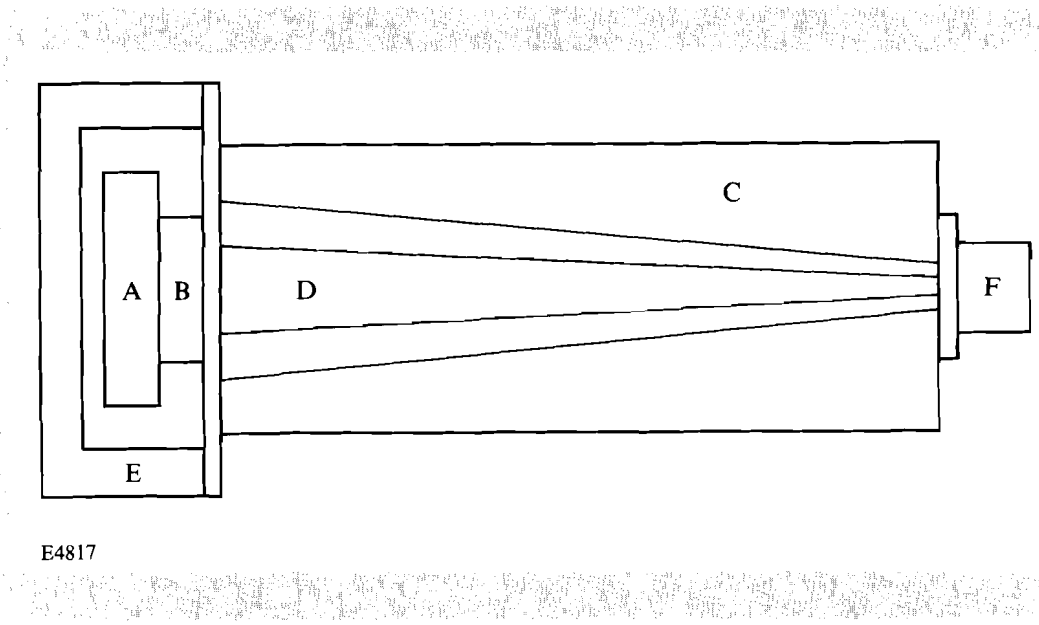

Fig. 36.11
Neutron time-of-flight detector (cross section). (A) scintillator, BC-422; (B) ITT f4129 PMT; (C) outer housing; (D) inner coaxial line; (E) lead x-ray shielding; (F) output connector.

In summary, we have employed a number of cross-checked detectors on recent experiments to measure neutron yield, shell areal density, fuel areal density, and fuel-ion temperature. Where possible, multiple detectors are used to measure important parameters, such as primary neutron yield.

ACKNOWLEDGMENT

This work was supported by the U. S. Department of Energy Office of Inertial Fusion under agreement No. DE-FC08-85DP40200 and by the Laser Fusion Feasibility Project at the Laboratory for Laser Energetics, which has the following sponsors: Empire State Electric Energy Research Corporation, New York State Energy Research and Development Authority, Ontario Hydro, and the University of Rochester. Such support does not imply endorsement of the content by any of the above parties.

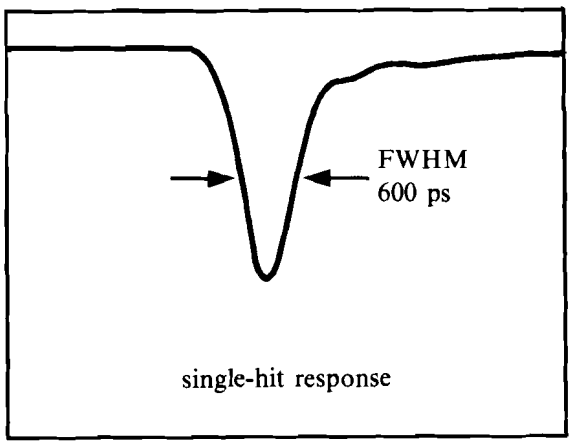

Fig. 36.12
Neutron time-of-flight detector output pulse.

REFERENCES

1. LLE Review **27**, 103 (1986).
2. S. M. Lane, E. M. Campbell, and C. Bennett, *Appl. Phys. Lett.* **37**, 600 (1980).
3. E. G. Gamalii *et al.*, *JETP Lett.* **21**, 70 (1975).
4. T. E. Blue and D. B. Harris, *Nuc. Sci. Eng.* **77**, 463 (1981).
5. M. D. Cable and S. P. Hatchett, *J. Appl. Phys.* **62**, 2233 (1987).
6. H. Azechi *et al.*, *Appl. Phys. Lett.* **49**, 555 (1986).
7. *Radiation Detection and Measurement*, edited by G. F. Knoll (Wiley and Sons, NY, 1979), pp. 576-584.
8. H. Brysk, *Plasma Phys.* **15**, 611 (1973).

1.D Beam Smoothing by Spectral Dispersion (SSD)

Techniques for improving laser beam uniformity currently involve breaking up the beam into a large number of beamlets whose diffraction-limited size is roughly the same as the target diameter. The resultant intensity pattern on target will be a smooth envelope superimposed upon a rapidly varying interference pattern from the overlap of the different beamlets. In the approach proposed by Kato[1] it is assumed that much of the interference structure would be eliminated by thermal smoothing within the target or by refraction of the beamlets in the target atmosphere. It is unlikely, however, that the very-long-wavelength structure will be eliminated. To eliminate nearly all the interference structure, a group at the Naval Research Laboratory has proposed the scheme of induced spatial interference (ISI)[2–4] whereby each beamlet is delayed by one or more coherence times so that the interference pattern on target fluctuates in time, resulting in a smooth time-averaged intensity profile. This technique requires a spectrally broad laser pulse (i.e., a short coherence time) to achieve smoothing in a time smaller than the characteristic hydrodynamic time scale of the target. However, due to the narrow spectral bandwidth required to achieve high-efficiency frequency tripling, the application of ISI has to date been ruled out for a frequency-tripled system such as OMEGA or NOVA. Two alternative approaches[5,6] also require a spectrally broad laser pulse.

We are proposing a new technique to smooth the interference pattern and still permit frequency tripling (or quadrupling). Like ISI, a broad bandwidth is required, but the spectrum is now dispersed spatially. Smoothing of the interference pattern is now achieved by the rapid temporal oscillations that result from the interference of the beamlets of different frequency. This smoothing may be faster than the superposition of the random intensity patterns achieved in ISI. Further, if the laser pulse can be spatially coded with a linear spectral variation, it is possible to achieve high-frequency tripling performance by simply compensating for the spectral variation with a linearly varying angle of incidence on the frequency converter. The spectral encoding can be accomplished, for example, by the use of dispersive optics such as gratings, while the angle-of-incidence variation can be achieved by the imposition of cylindrical divergence or convergence on the beam.

A possible use of this approach to reduce the modulation produced by the interference of distributed phase plate (DPP) beamlets on target is shown schematically in Fig. 36.13. A broadband pulse, produced either by a broadband oscillator or by propagation of a narrow-bandwidth pulse through a fiber or a suitable nonlinear medium, is dispersed spectrally with a pair of gratings producing a beam of approximately rectangular cross section with linear variation in wavelength along the long direction. After correction of the beam shape with appropriate cylinder optics and apodizing aperture, the beam is propagated through the normal amplifier system. Prior to frequency conversion a weak cylindrical lens imposes a matched convergence to the beam, which is corrected with a negative lens

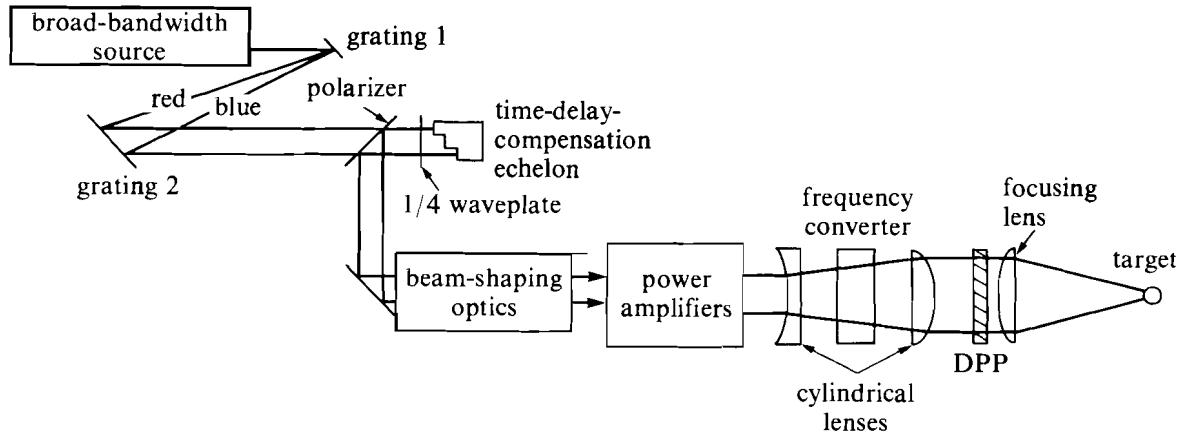

Fig. 36.13
Schematic of beam-smoothing system using spectral dispersion.

following the frequency converter. As an example, to compensate for a 10-Å variation in wavelength in one direction, a convergence (or divergence) of 1.6 mrad is required. The existing DPP's are used in conjunction with the spectrally broadened pulse to achieve nearly modulation-free beam envelopes for times much longer than the pulse mutual coherence time.

Computer code simulations of the interference pattern generated by the DPP's show that for times larger than 25 - 50 coherence times the beam pattern on target is nearly modulation free. This is the result of a spectral variation along only one direction (chosen to match the crystal cut). If we require this smoothing time to be of order 25 ps to 50 ps, a bandwidth of approximately 10^{12} Hz is required at 0.35 μm, which corresponds to 10 Å at 1.054 μm (frequency tripling increases the pulse bandwidth by a factor of 3 in frequency). Since the gain bandwidth of the most commonly used laser glass, LHG-8, is 218 Å (FWHM), the energy capability of the high-power glass laser should not be reduced substantially by the increased bandwidth.

Broad-Bandwidth Generation

There are a number of alternative ways to generate a laser pulse with broad spectral bandwidth. The conventional ISI technique typically makes use of a Q-switched oscillator with appropriate intracavity etalons to generate the desired spectral content. The typical bandwidth generated by such oscillators is 100 Å or less. These oscillators produce pulses several tens of nanoseconds long and must therefore be further shortened by a pulse-chopping system.[2,6]

An alternative approach is to create the spectral broadening external to the oscillator. Through a combination of self-focusing and self-phase

modulation it is possible to obtain large spectral broadening and chirping by propagating an intense pulse through an optical fiber.[7] The degree of broadening and chirping is a function of the pulse energy, the pulse width, and the fiber length. This technique for bandwidth generation has the disadvantage of requiring a high degree of control on the input pulse parameters and is relatively inflexible.

Spectral broadening has been demonstrated by the use of an electro-optic phase modulator[8]; spectral bandwidths up to 600 GHz were demonstrated with a $LiTaO_3$ modulator driven by a 9.35-GHz, pulsed-microwave generator. This appears to be a promising way to broaden the spectral content of bandwidth-limited laser pulses.

Spectral Dispersion

Gratings offer the best technique for achieving the required levels of spectral dispersion. Using a linear grating where the first order diffracts close to retroreflection,[9] high reflectivity may be achieved.

Consider a beam incident on a grating with line spacing d at an angle θ_i to the plane of the grating (Fig. 36.14). The grating equation relates the diffraction angle θ_r and the wavelength λ by

$$\lambda = d[\cos\theta_i + \cos\theta_r(\lambda)] \ .$$

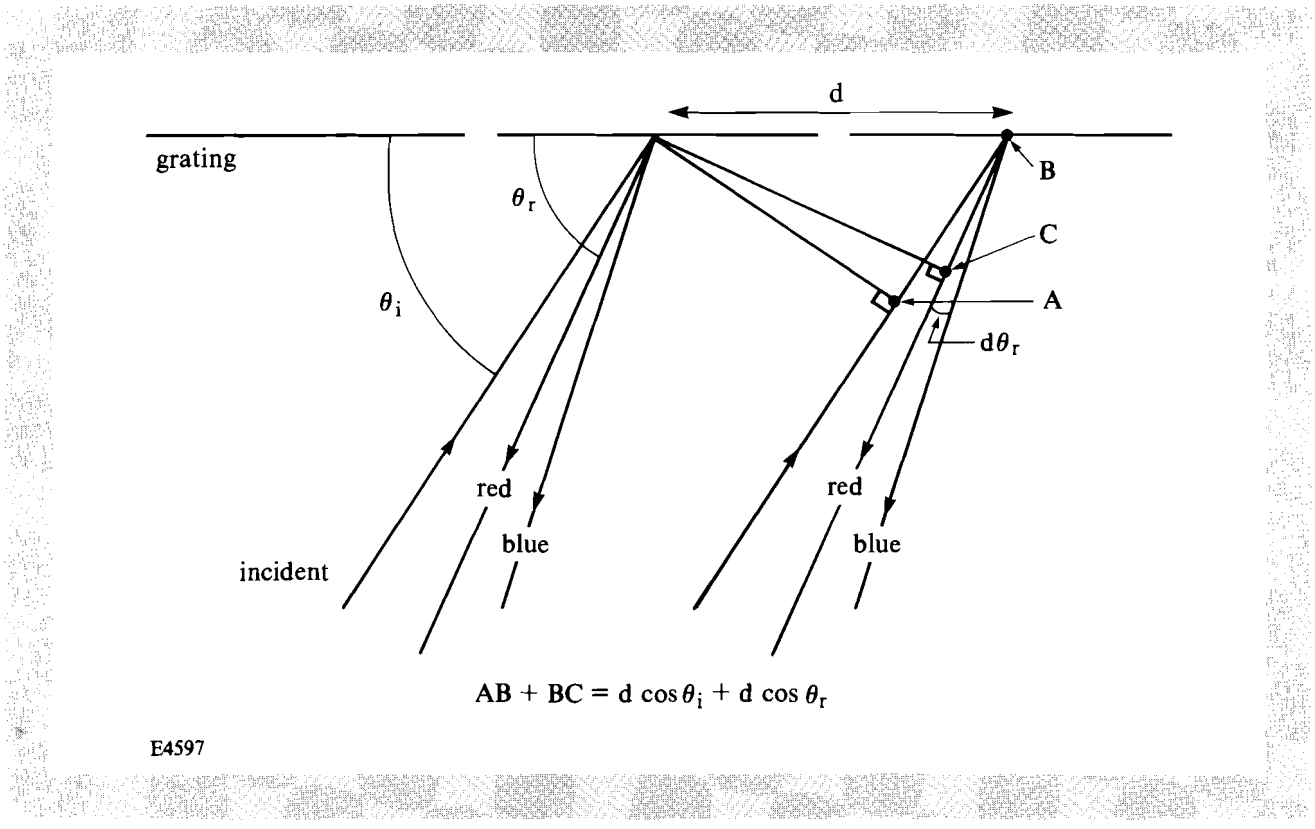

Fig. 36.14
Diffraction grating operated in first order close to retroreflection. The optical path difference between the red rays is shown as $AB + BC$. The blue rays emerge closer to the grating normal.

If $\lambda = \lambda_o + \Delta\lambda$ where $\lambda_o = 2d\cos\theta_o$, θ_o being the retro-angle for the central wavelength λ_o, then

$$\cos\theta_r(\lambda) = \frac{\lambda(2\cos\theta_o)}{\lambda_o} - \cos\theta_i \quad .$$

Differentiating, we obtain $\sin\theta_r \frac{d\theta_r}{d\lambda} = \frac{2\cos\theta_o}{\lambda_o}$,

so that

$$d\theta_r = -a\frac{d\lambda}{\lambda_o} \quad , \tag{1}$$

where $a \equiv 2\cos\theta_o/\sin\theta_r$. For typical conditions ($d = 0.588$ μm, $\lambda_o = 1.054$ μm, $\theta_r \approx \theta_o = 26.38°$), we have $a = 4.033$. If $\Delta\lambda = 10$ Å, $d\theta_r \simeq 4 \times 10^{-3}$ rad. Prisms would be unsuitable as they give dispersions about two orders of magnitude smaller.

To obtain efficient frequency tripling with this approach, we must have relatively high spectral dispersion so that the bandwidth of the dispersed beam at any one point $\lesssim 1$ Å. We can estimate the requirements on beam size D and grating separation L, using the construction shown in Fig. 36.15.

If the source spectrum contains wavelengths from λ_o to $\lambda_o + d\lambda_{max}$, and the resulting dispersion spreads the spectrum in the plane of the second grating over a length y_{max}, then

$$y_{max} \simeq Ld\theta_r \quad , \tag{2}$$

it being assumed that we are operating close to retroreflection, and

$$\lambda(y) = \lambda_o + (y/y_{max})\, d\lambda_{max} \quad .$$

At a point y, we see all wavelengths between $\lambda(y + D/2)$ and $\lambda(y - D/2)$, i.e., between

$$\lambda_o + \frac{y}{y_{max}} d\lambda_{max} \pm \frac{D}{2y_{max}} d\lambda_{max}$$

or

$$\lambda(y) \pm \frac{\delta\lambda}{2}$$

where

$$\delta\lambda = \frac{D}{y_{max}} d\lambda_{max} \quad . \tag{3}$$

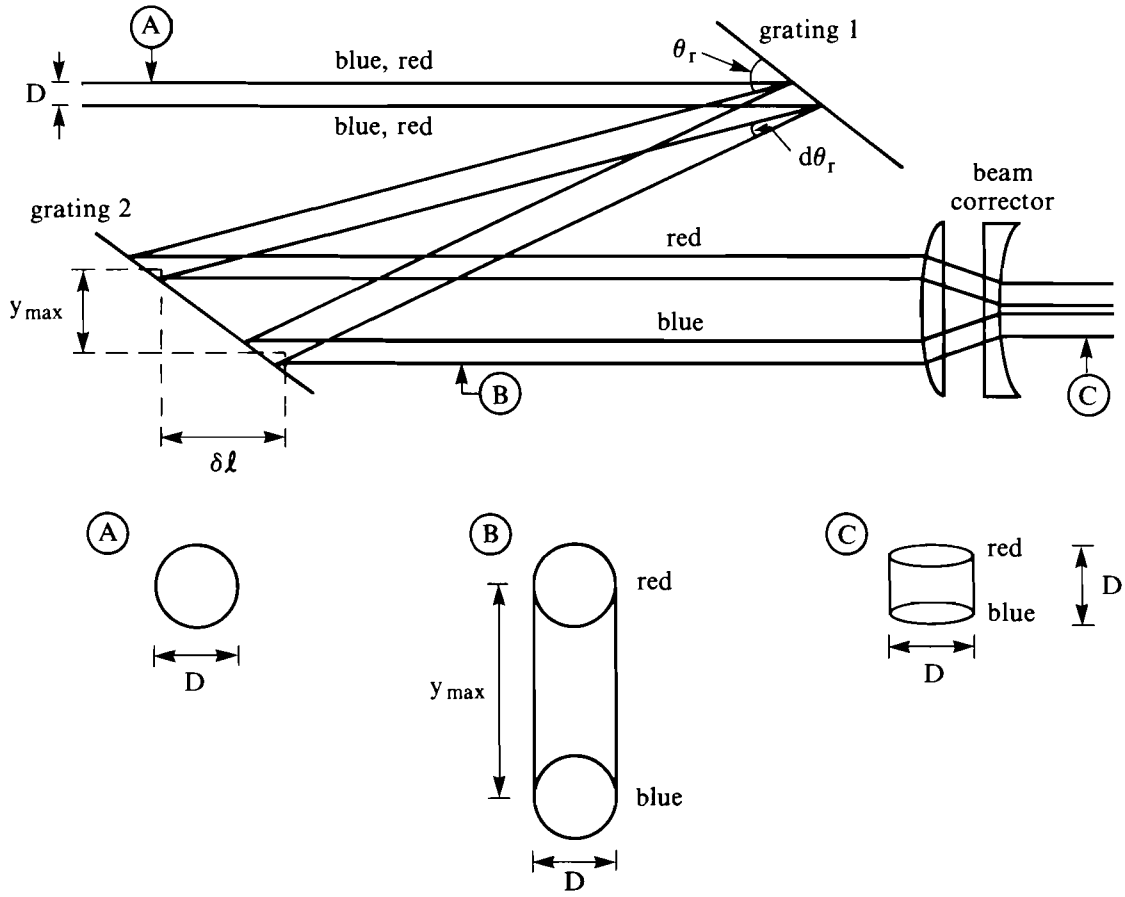

Fig. 36.15
Schematic showing change of beam shape while passing through a grating pair followed by a cylindrical collimator used to correct the beam shape. The time delay of the red component relative to the blue is approximately 2 $\delta\ell$.

Thus, the bandwidth is reduced after dispersion by the factor y_{max}/D, known hereafter as the spatial dispersion factor, the same factor by which the beam cross-section is elongated. For example, if $d\lambda_{max}$ = 10 Å, $\delta\lambda$ = 1 Å, and D = 0.3 cm, then y_{max} = 3 cm. Note that the grating separation required is determined by $\delta\lambda$ and not $d\lambda_{max}$ since [from Eqs. (1)-(3)]

$$\frac{D}{L} = a\,\frac{\delta\lambda}{\lambda_o} \quad .$$

In our case, with the requirement that $\delta\lambda/\lambda_o < 10^{-4}$ for high-frequency tripling, $D/L < 4 \times 10^{-4}$ regardless of $d\lambda_{max}$. For example, with D = 0.3 cm, we require $L > 7.5$ m.

The Effect of Diffraction

The beam diameter D spreads laterally with characteristic half-angle ϕ given by $\phi \sim \lambda_0/D$, and must be chosen to be sufficiently large that the added bandwidth is less than $\delta\lambda$.

After propagation through a distance L, the beam half-width increases by $\sim L\phi$. In order to avoid added bandwidth at distance L we require $L\phi < D$, i.e., $L\lambda_0 < D^2$,

or

$$\frac{D}{\lambda_0} > \frac{L}{D} = \frac{1}{a}\frac{\lambda_0}{\delta\lambda}$$

or

$$D > \lambda_0 \left(\frac{1}{a}\frac{\lambda_0}{\delta\lambda}\right).$$

For $\delta\lambda/\lambda \lesssim 10^{-4}$ and $a \approx 4$, $D > 0.25$ cm, so that the assumed $D = 0.3$ cm is just large enough and we may have to increase D to say 0.5 cm to assure high spectral purity.

Beam Temporal Spread

As may be evident from Fig. 36.15 the double-grating spectral disperser introduces a time delay across the beam that is linearly proportional to the imposed bandwidth. The red edge of the beam is delayed relative to the blue edge by a distance given approximately by

$$2\,\delta\ell = 2\,y_{max}\cot\theta_0 \approx a\,y_{max}\ ,$$

which, in our example ($y_{max} = 3$ cm), is 12 cm or 400 ps. Since DPP's are to be used for phase conversion in the proposed smoothing technique, this temporal delay eventually results in an effective temporal broadening of the pulse. One method of correcting for this delay is to employ appropriately designed echelons at the output of the grating disperser as shown in Fig 36.13.

Frequency-Conversion Requirements

Table 36.II summarizes the requirements imposed on beam alignment and wavelength when performing frequency tripling using two KDP crystals of equal length. Data is given for fourth-harmonic generation for completeness.[10]

The angular acceptance and bandwidth are often quoted in terms of the FWHM's $\Delta\theta_{FWHM}$ and $\Delta\lambda_{FWHM}$. It is important to note that these quantities relate to the "tuning curves" obtained for monochromatic, unidirectional beams propagated at a varying wavelength or angle. The cases involving a broadband beam, or a beam containing large intrinsic divergence (a spread of angles), are more complicated as they entail nonlinear interactions between the different modes that can lead to the introduction of broadening and structure to the k and ω spectra.[12]

Table 36.II
Sensitivity of conversion crystals to errors in angle and wavelength.

	$\Delta\theta_{FWHM}$ mrad	$\Delta\lambda_{FWHM}$ Å	$\Delta\theta/\Delta\lambda$ mrad/Å	$\Delta\theta_{90}$[(c)] mrad	$\Delta\lambda_{90}$[(c)] Å
Tripler (type-II KDP)[(a)]					
1 cm, small signal	1.560	9.554	−0.163	0.312	1.911
1.6 cm, small signal	0.975	5.971	−0.163	0.195	1.194
1.6 cm, high conversion[(d)(f)]	0.488	2.986	−0.163	0.098	0.597
Doubler (type-II KDP)[(a)]					
1 cm, small signal	3.207	154.485	−0.021	0.641	30.897
1.6 cm, small signal	2.004	96.553	−0.021	0.401	19.311
1.6 cm, high conversion[(e)(f)]	2.004	96.553	−0.021	0.401	19.311
Quadrupler (type-I KDP)[(b)]					
1 cm, small signal	1.985	1.363	−1.453	0.397	0.273

Notes:

(a) Optimum operating intensities for tripling are 4 GW/cm^2 (1-cm doubler and tripler) and 1.5 GW/cm^2 (1.6-cm doubler and tripler).

(b) Frequency quadrupling would probably be done with thickness 0.5–1.0 cm depending on two-photon absorption constraint.

(c) $\Delta\theta_{90}$ = shift from peak, which gives 90% of peak conversion. Table uses $\Delta\theta_{90} = 0.2\ \Delta\theta_{FWHM}$; similarly for $\Delta\lambda$.

(d) Use half the small-signal values; this applies when approximately 80% overall conversion is achieved.

(e) Use small-signal values for sensitivity of overall tripling to doubler errors. This is an attractive feature of the polarization-mismatch scheme.[11]

(f) Values quoted are not greatly different between single rays and averages over a temporal Gaussian.

(g) All angles are measured in air.

E4811

The quantities $\Delta\theta_{FWHM}$ and $d\lambda_{FWHM}$ are inversely proportional to the crystal thickness. The ratio $\Delta\theta/\Delta\lambda = n\ d\theta_m/d\lambda$, where n is the refractive index of KDP, is proportional to the rate of change of phase-matching angle θ_m with respect to λ, and is independent of crystal thickness or operating intensity.

Suppose that the crystals are tuned to the phase-matching angle corresponding to a given wavelength. The quantities $\Delta\theta_{90}$ and $\Delta\lambda_{90}$ are the shifts in angle (exterior to the crystal) and wavelength that reduce the conversion efficiency to 90% of its peak value. To a good

approximation, they are a factor of 5 smaller than the FWHM's. Near the peak of the tuning curve the relationship is close to quadratic: e.g., shifts of $\Delta\theta_{90}/3$ or $\Delta\lambda_{90}/3$ would reduce the efficiency by 1%. These values would be important for the reproducibility of a system with, say, a requirement of 1% beam balance. For tripling with our current 1.6-cm crystals, $\Delta\theta_{90} = 98$ μrad and $\Delta\lambda_{90} = 0.597$ Å.

Correction of the phase-matching angle for a beam whose wavelength λ_0 shifts linearly in one direction across the cross section is easily performed using a pair of weak cylindrical lenses, as shown in Fig. 36.16. These lenses could be used as windows for the conversion cell. At each point y in the beam the spectrum has a peak λ_0 (y), which is a linear function of y, and a width $\delta\lambda$, which is independent of y. For example, for a spatial dispersion factor (y_{max}/D) of 10, a variation of λ_0 by $d\lambda_{max} = 10$ Å across the beam implies $\delta\lambda = 1$ Å, so that locally the spectrum is $\lambda_0(y)\pm 0.5$ Å. The local spectral width is (just) within the $\Delta\lambda_{90}$ of our current system, and so we would expect minimal degradation of conversion, although the actual degradation (resulting from the nonlinear mode-mode interactions mentioned above) could be greater. This degradation would be uniform across the beam aperture. In spite of this uncertainty, 1 Å seems a reasonable value to require for $\delta\lambda$. From Table 36.II, the half-angle Ψ of decollimation = 0.163 $(d\lambda_{max}/2)$ = 0.815 mrad.

The doubler tuning is unaffected by this decollimation, since the sensitive direction of the doubler is orthogonal to that of the tripler. (If instead we were to use a spherical decollimation, rays at the edges of the doubler would be mismatched by 0.815 mrad, about 2 $\Delta\lambda_{90}$, leading to non-negligible losses in these regions.) The wavelength error incident on the doubler, ± 5 Å in our example, is well within $\Delta\lambda_{90} = 19$ Å, so the doubling efficiency is not compromised. The doubler bandwidth does, however, limit the maximum feasible $d\lambda_{max}$, with 10% at the edge of the beam (2.5% overall) lost when $d\lambda_{max} =$ 40 Å. Larger bandwidths than this would not propagate satisfactorily (i.e., with uniform amplification in the frequency domain) through the system due to the finite gain bandwidth of Nd:glass.

The wavelength acceptance of KDP for fourth-harmonic generation is several times smaller; one would then need a much larger spatial dispersion factor to achieve the same $d\lambda_{max}$.

Propagation Issues

Some issues associated with the successful propagation of a spectrally dispersed beam are discussed in this section.

1. Diffraction

Figure 36.15 shows how the shape of the beam cross section changes from point A (input to gratings G_1 and G_2), to point B (output from gratings), and to point C (after reshaping to a circular cross section). At A, all frequency components in the original beam overlap spatially and are assumed to have a flat phase front. Each component propagates along a different path through the gratings (and through or

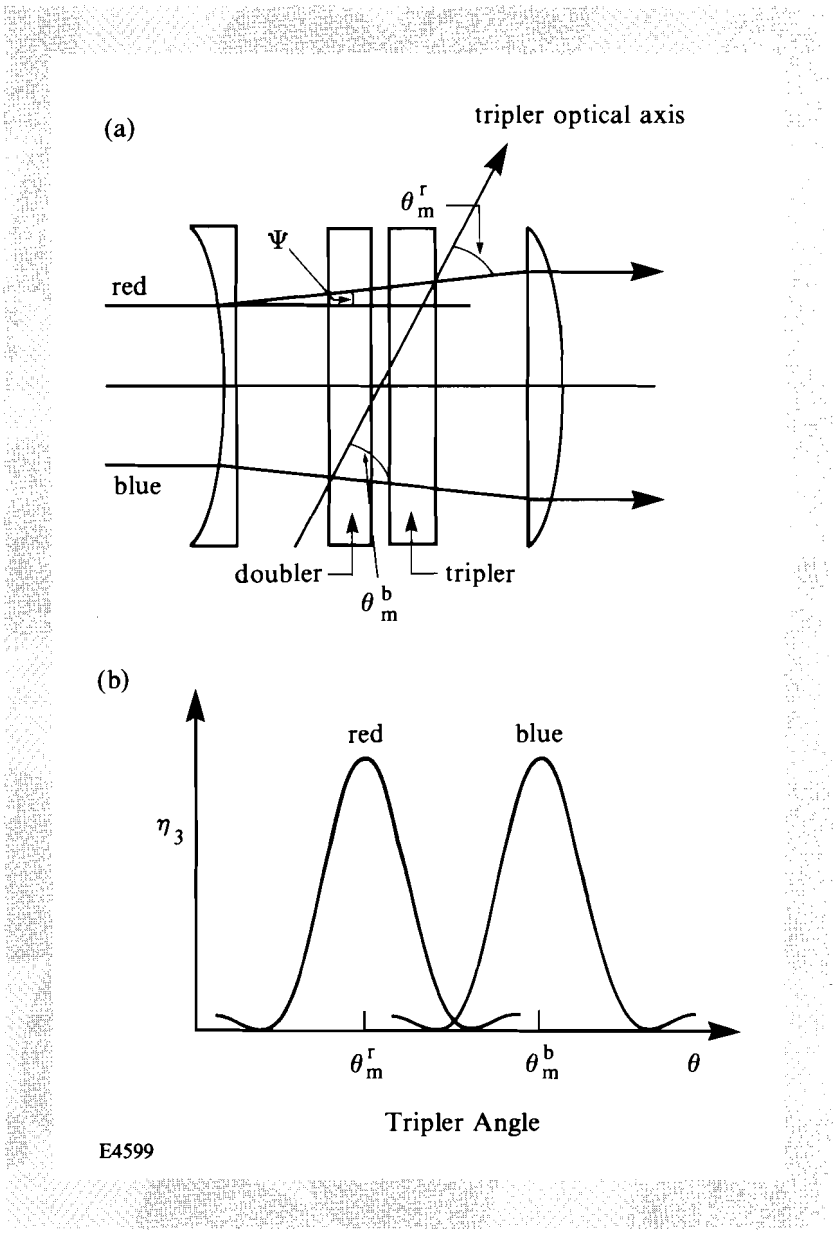

Fig. 36.16
Correction of phase-matching angle for a beam whose spectrum varies linearly across the beam aperture: (a) the imposition of a cylindrical divergence causes the red and blue portions of the spectrum to make different angles with the tripler optic axis; (b) overall third-harmonic conversion efficiency, η_3 as a function of the angle between the beam and the tripler optic axis. The optimum angle θ_m varies linearly with frequency.

reflected off an echelon or another diffractive element, not shown or specified here, to compensate for the time delay of the red component), maintaining its circular shape and size if diffraction spreading is small. After beam reshaping (point *C*) the resultant beam is approximately square, but could be apodized to circular if desired.

Each frequency component occupies an elliptical cross section, with width reduced by the spatial dispersion factor. This reduced width will result in increased diffraction spreading as this component propagates through the system. For this reason the limit of complete spatial dispersion ($\delta\lambda \rightarrow 0$), which has some interesting and unusual features, is unattainable. Whether diffraction is a problem for the spatial dispersion factors of order 10 under consideration remains to be determined.

2. Divergence

If diffraction can be neglected, good propagation through the system requires that each frequency component have a flat phase front across the beam aperture. This is especially important because the beam reshaping will cause phase errors to occur across a smaller transverse distance; equivalently, the intrinsic divergence in the direction of spectral dispersion is increased by the spatial dispersion factor. This is a concern for frequency conversion, which is sensitive to divergence: from Table 36.II, $\Delta\theta_{90} = 100$ μrad for our current crystals at high conversion.

3. Source of Broad-Bandwidth Input

The physical means by which the broad bandwidth is produced are important. Consider first a frequency-chirped pulse, such as is produced by an optical fiber where, approximately, the frequency increases linearly during the pulse, and assume that the relative path-length delay through the gratings has been corrected. On examination of the beam shape at point *C* in Fig. 36.15, the energy in the beam would be delivered in an elliptical subaperture that would move across the beam in time. This would be unacceptable for two reasons: (a) instantaneous intensities would be increased by the spatial dispersion factor (say 10), and (b) the focusing lens would see only one frequency at each time, thereby voiding the desired interference between frequencies. There is a related problem: if for some reason the input pulse were produced without the broad bandwidth, it would propagate through the system with ten times the desired intensity. It is therefore highly desirable that the frequency spectrum of the input be uniform throughout the pulse, and spread uniformly between $\lambda_0 \pm d\lambda/2$, in order to avoid operating with an unacceptably low fill factor.

One theoretical possibility might be to spectrally disperse a longer pulse (say 10 ns) through a fiber, so that each frequency component would have the desired duration ($\sim$1 ns), and then impose large relative delays ($\sim$10 ns or 3 m) on the red portion of the spectrum to bring the components together in time. This seems to be impractical, not least because Raman scattering prevents the use of fibers in this regime.

Another possibility might be to propagate a discrete number of different frequencies, each assigned to a discrete portion of the beam. In order to obtain good on-target smoothing, a large number ($\gtrsim$ 50 ?) of such frequencies would be needed, since otherwise time-independent phase relationships would be maintained over large spatial regions of the focusing lens.

4. Interference Effects

Interference effects in the laser between overlapping spectral components have not yet been considered. The simple model we have implicitly assumed, whereby individual Fourier components propagate independently until they add in the target plane to give the target irradiation pattern, is valid for propagation through linear elements in the laser chain but may not provide a correct treatment of nonlinear processes such as self-focusing and frequency conversion.

Calculations of Beam Smoothing

Consider a beam propagating in the z-direction that passes through a random phase mask (RPM) with square elements of diameter d and is focused at a distance F from the mask. For simplicity assume the beam has a constant near-field amplitude. Then the electric field E in the target (focal) plane is given by[13]

$$E(x,y) \sim \operatorname{sinc}\left(\frac{xd}{\lambda F}\right) \operatorname{sinc}\left(\frac{yd}{\lambda F}\right) \times Re\sum_{k,\ell} \exp\left[-\frac{2\pi}{\lambda F} i(X_k x + Y_\ell y) + i\phi_{k\ell} + i\tilde{\phi}_{k\ell}(t)\right], \quad (4)$$

where (k, ℓ) refer to an individual element of the RPM, (X_k, Y_ℓ) is the center of the element measured from the beam axis, and $\phi_{k\ell}$ is the static phase imposed on the beam. The spatially dispersed spectrum introduces an additional phase variation across the beam, which is assumed to be of the form

$$\tilde{\phi}_{k\ell}(t) = \omega_0 t + \Delta\omega \frac{R+Y_\ell}{2R} t \quad ,$$

where R is the radius of the near-field beam, and $\Delta\omega$ is the spread in frequency. It should be noted that this is a highly simplified model, since it neglects the overlap at each point on the near field of a range of Fourier components.

The intensity I will vary as $|E|^2$. Separating out the phase terms and neglecting terms that vary as $2\omega_0 t$, we have

$$I(x,y,t) = I_0(x,y) x \sum_{\substack{k,\ell \\ m,n}}^{N} \cos\left\{-\frac{2\pi}{\lambda F}[(X_k - X_m)x + (Y_\ell - Y_n)y] + (\phi_{k\ell} - \phi_{mn}) + \frac{\Delta\omega t}{2R}(Y_\ell - Y_n)\right\}, \quad (5)$$

where N is the number of phase plate cells in one direction. The target will respond to the time-average intensity, averaged over the characteristic hydrodynamic time scale. The average is

$$\bar{I}(x,y,t) = \frac{1}{t}\int_0^t I(x,y,t')\,dt'$$

$$= N^2 I_0(x,y) + I_0 \sum_{\substack{k\neq m \\ \ell}} \cos\left[\frac{-2\pi}{\lambda F}(X_k - X_m)\,x + (\phi_{k\ell} - \phi_{m\ell})\right]$$

$$+ \frac{1}{\Delta\omega t} I_0 \sum_{\substack{\ell\neq n \\ k\neq m}} \left[\frac{2R}{Y_\ell - Y_n} \sin\left[-\frac{2\pi}{\lambda F}(X_k - X_m)\,x + (\phi_{k\ell} - \phi_{mn})\right.\right.$$

$$\left. + \left(\frac{\Delta\omega t}{2R} - \frac{2\pi}{\lambda F} y\right)(Y_\ell - Y_n)\right]$$

$$\left. - \frac{2R}{Y_\ell - Y_n} \sin\left\{-\frac{2\pi}{\lambda F}\left[(X_k - X_m)\,x + (Y_\ell - Y_n)y\right] + (\phi_{k\ell} - \phi_{mn})\right\}\right]. \quad (6)$$

Part of the interference term is seen to decrease as $1/\Delta\omega t$. Further, the effect of time averaging is found to be similar to the effect of a one-dimensional spatial average in the direction of wavelength dispersion. Temporal smoothing is most rapid for interference between beams produced the furthest apart ($Y_\ell - Y_n$ the largest), which produces the short-wavelength structure. The long wavelength is reduced on a longer time scale. This is illustrated in Figs. 36.17–36.20, which show horizontal and vertical cuts through the far-field (target-plane) beam for $\Delta\omega t/2\pi = 1$, 10, 25, and ∞, respectively. For the example of a 10-Å bandwidth in the IR, the first three correspond to averaging times approximately of 1, 10, and 25 ps.

There will always be a residual interference variation along the direction perpendicular to the wavelength dispersion, as seen in Fig. 36.20 ($t = \infty$) and Eq. (6). The oscillations around the smooth envelope have peak-to-valley variations of about $1/\sqrt{N}$). The example in Fig. 36.20 uses a 100 × 100 phase plate, and the resultant peak-to-valley oscillations are ±5%.

ACKNOWLEDGMENT

This work was supported by the U. S. Department of Energy Office of Inertial Fusion under agreement No. DE-FC08-85DP40200 and by the Laser Fusion Feasibility Project at the Laboratory for Laser Energetics, which has the following sponsors: Empire State Electric Energy Research Corporation, New York State Energy Research and Development Authority, Ontario Hydro, and the University of Rochester. Such support does not imply endorsement of the content by any of the above parties.

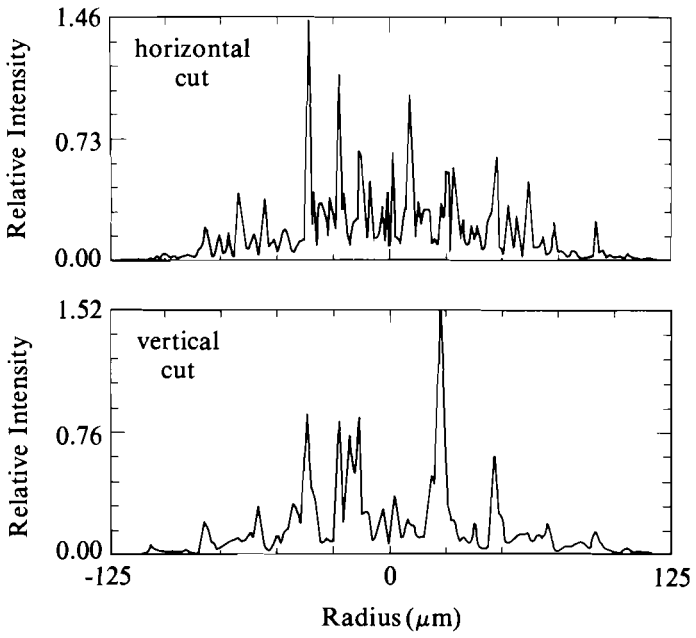

Fig. 36.17
Calculation of the effect of smoothing by spectral dispersion showing horizontal and vertical cuts through the far-field beam for $\Delta\omega t/2\pi = 1$.

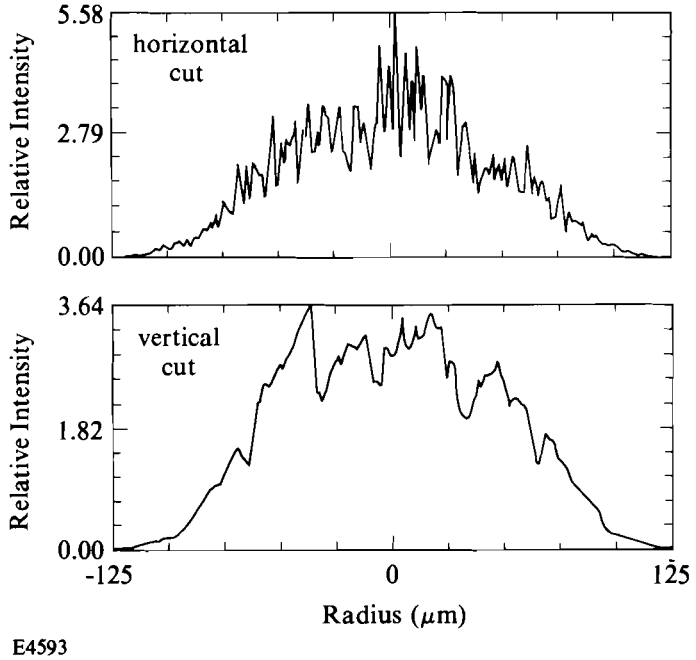

Fig. 36.18
Same as Fig. 36.17 with $\Delta\omega t/2\pi = 10$.

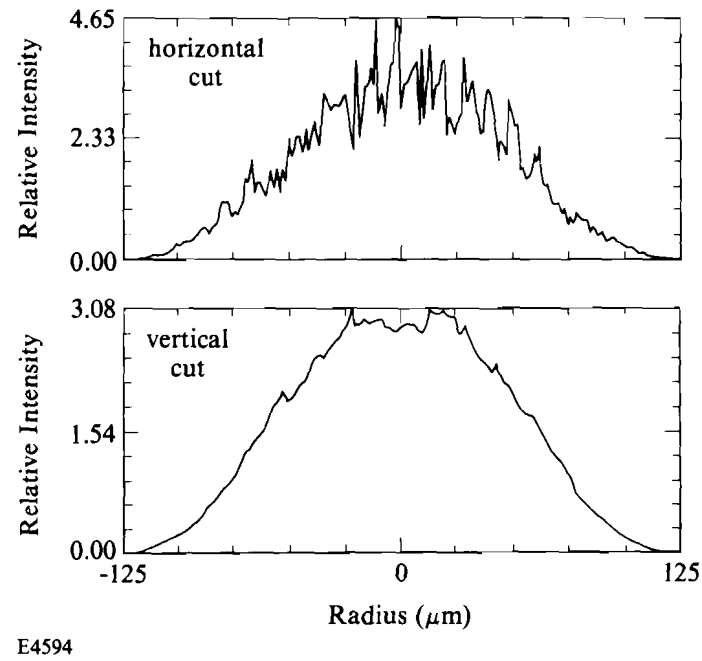

Fig. 36.19
Same as Fig. 36.17 with $\Delta\omega t/2\pi = 25$.

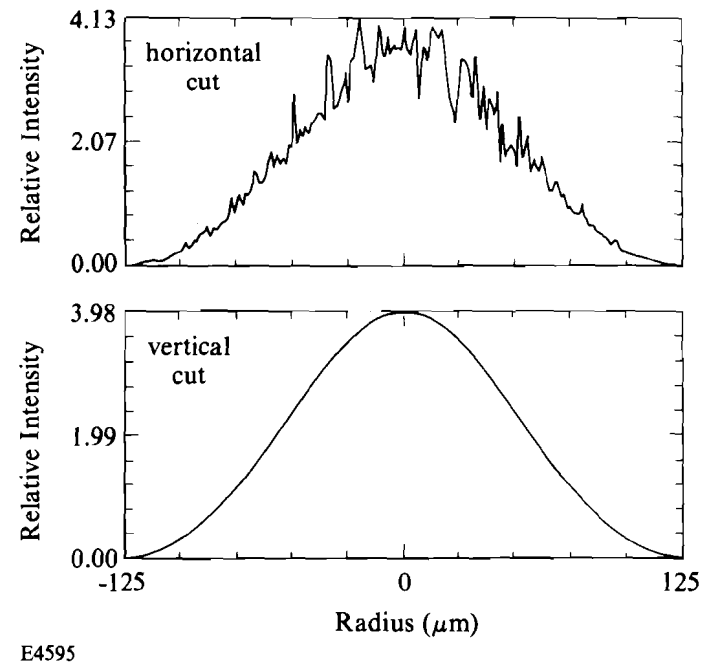

Fig. 36.20
Same as Fig. 36.17 with $\Delta\omega t/2\pi = \infty$.

REFERENCES

1. Y. Kato *et al.*, *Phys. Rev. Lett.* **53**, 1057 (1984).
2. R. H. Lehmberg and S. P. Obenschain, *Opt. Commun.* **46**, 27 (1983).
3. S. P. Obenschain *et al.*, *Phys. Rev. Lett.* **56**, 2807 (1986).
4. R. H. Lehmberg, A. J. Schmitt, and S. E. Bodner, *J. Appl. Phys.* **62**, 2680 (1987).
5. R. H. Lehmberg and J. Goldhar, *Fusion Tech.* **11**, 532 (1987).
6. D. Veron *et al.*, *Opt. Commun.* **65**, 42 (1988).
7. R. R. Alfano and P. P. Ho, *IEEE J. Quantum Electron.* **24**, 351 (1988).
8. T. Kobayashi *et al.*, *IEEE J. Quantum Electron.* **24**, 382 (1988).
9. E. B. Treacy, *IEEE J. Quantum Electron.* **QE-5**, 454 (1969).
10. R. S. Craxton, S. D. Jacobs, J. E. Rizzo, and R. Boni, *IEEE J. Quantum Electron.* **QE-17**, 1782 (1981).
11. R. S. Craxton, *IEEE J. Quantum Electron.* **QE-17**, 1771 (1981).
12. R. C. Eckardt and J. Reintjes, *IEEE J. Quantum Electron.* **QE-20**, 1178 (1984).
13. M. Born and E. Wolf, *Principles of Optics*, 6th corrected ed. (Pergamon Press, New York, 1980), pp. 436–437.

1.E Two-Dimensional, Nonlocal Electron Transport in Laser-Produced Plasmas

Much effort has been devoted to the study of nonlocal electron transport in laser-produced plasmas.[1,2] Most of the work has involved the numerical solution of the electron Fokker-Planck (FP) equation in one dimension by finite difference techniques. Comparisons with standard fluid transport calculations using Spitzer-Härm (SH)[3] heat flow $\underset{\sim}{q}_s = -\kappa \underset{\sim}{\nabla} T$ has revealed the occurrence of hot-electron "preheat," as well as reduced penetration of the bulk heat front, a phenomenon known as "flux inhibition."[1] To simulate the latter effect, fluid codes are normally equipped with an artificial flux limiter, which maintains the heat flux $\underset{\sim}{q}$ below some fraction f of its free-streaming limit $q_f = nm(T/m)^{3/2}$, i.e., $\underset{\sim}{q} = \underset{\sim}{q}_s/(1 + |\underset{\sim}{q}_s/fq_f|)$.[4,5]

This technique has been shown to be adequate for long-pulse ($\sim$ 1-ns), short-wavelength ($<$ 1-μm) lasers at moderate irradiances ($< 10^{15}$ W/cm^2), where usually $q_s \lesssim fq_f$ (for f = 0.1–0.2).[6] However, if the transport is two-dimensional (2-D), as would be the case for nonuniformly illuminated laser plasmas, the validity of fluid theory has not yet been tested. In particular, the application of flux limiters

requires special care, since the direction of the heat flow may not always be parallel to $-\nabla T$.[5,7] Nevertheless, 2-D fluid codes are widely used for thermal transport studies with each direction individually flux limited.[8]

Here, we investigate the validity of the fluid modeling by constructing a code (SPARK) designed to numerically solve the electron *FP* equation in 2-D planar geometry under conditions relevant to laser-produced plasmas. By imposing a spatial inhomogeneity of scale ℓ in the incident laser beam, we show that the nonlocal electron transport is less effective at smoothing temperature gradients than the corresponding diffusive transport based on *SH* heat flow, irrespective of the size of the flux limiter. This effect becomes significant when $\ell \lesssim 80\lambda_{mfp}$, where λ_{mfp} $(= 3T^2/4\sqrt{2\pi}\, Zne^4 \ln\Lambda)$ is the electron-ion mean free path at the critical surface.

The numerical algorithm of SPARK is briefly described as follows (for further details see Ref. 7). Using the diffusive approximation and taking the high-Z limit of the *FP* equation, we obtain (using the notation of Shkarofsky, Johnston, and Bachynsky)[9]

$$\frac{\partial f_o}{\partial t} + \frac{v}{3}\nabla\cdot\underset{\sim}{f}_1 = \frac{1}{v^2}\frac{\partial}{\partial v}\left[\frac{v^2}{3}\,\underset{\sim}{a}\cdot\underset{\sim}{f}_1 + Y\left(Cf_o + D\frac{\partial}{\partial v}f_o\right) + \frac{YnZ}{6v}v_o^2\frac{\partial}{\partial v}f_o\right], \tag{1a}$$

$$\underset{\sim}{f}_1 = -\tau\left(v\nabla f_o - \underset{\sim}{a}\frac{\partial}{\partial v}f_o\right), \tag{1b}$$

where

$$\underset{\sim}{a} = \frac{|e|}{m}\underset{\sim}{E},\quad \tau = v^3/[(Z+1)\,nY],\quad Y + 4\pi\,(e^2/m)^2\ln\Lambda,\quad C = I_o^o f_o,$$

$$\text{and } D = \frac{v}{3}\,(I_2^o + J_{-1}^o)\ .$$

To simplify the analysis, we have assumed the ions to be cold and motionless. The last term in Eq. (1a) is the inverse-bremsstrahlung operator, and v_o is the electron quiver velocity.[10] This reduced form of the *FP* equation has been successfully used for 1-D transport studies,[2] where one is not too interested in highly collisionless phenomena (such as Landau damping). Here, we have further neglected the effect of magnetic fields that may be justified by the fact that we will be comparing our results with fluid calculations based on the same approximation. Furthermore, we will simulate the transport under conditions where the effect of magnetic fields on the transport is not expected to be significant, i.e., short laser wavelength at moderate irradiances.[5]

Substituting Eq. (1b) into Eq. (1a) and defining

$$\alpha = -[\partial_v \ln(f_o)]/v,\ \underset{\sim}{\beta} = -\underset{\sim}{\nabla}\ln(f_o) \text{ and } \chi = v^2\tau/3,$$

we have

$$\frac{\partial f_o}{\partial t} = \underset{\sim}{\nabla} \cdot [\chi\,(\underset{\sim}{\nabla} f_o + \underset{\sim}{a}\alpha f_o)] + \frac{1}{v^2}\frac{\partial}{\partial v}\left\{\chi\left(\underset{\sim}{a}\cdot\underset{\sim}{a}\frac{\partial}{\partial v}f_o + v\underset{\sim}{\beta}\cdot\underset{\sim}{a}f_o\right) + Y\left[Cf_o + \left(D + \frac{nZv_o^2}{6v}\right)\frac{\partial}{\partial v}f_o\right]\right\}. \quad (2)$$

Assuming that the nonlinear coefficients α and $\underset{\sim}{\beta}$ are known explicitly, as is usually done with the terms $\underset{\sim}{a}$, C, and D, we have transformed the troublesome cross-derivatives into convective terms. The resulting diffusion-convection equation may now be solved by standard numerical techniques.

Equation (2) is differenced in conservative form by adopting Cartesian geometry in x, z, and v. A generalized Chang-Cooper[11] weighting is applied in all directions by using the zero flux condition across the cell boundaries. The electric field is calculated via the "implicit moment"[12] method by assuming that $\underset{\sim}{\nabla} \times \underset{\sim}{E} = 0$ and taking the

$$\int_0^\infty v^2 dv$$

moment of Eq. (2). (An alternative scheme that assumes the total current is zero and allows for a finite $\underset{\sim}{\nabla} \times \underset{\sim}{E}$ has also been tried with little effect on the transport calculations, apart from a deterioration in the quasi-neutrality.)[13] The resulting system of equations is solved by an "alternating-direction-implicit"[7,14] scheme in v, z, and x respectively, in conjunction with a "predictor-corrector" step. In the predictor stage, f_o is linearly extrapolated to the half-time level and used to calculate the nonlinear coefficients. In the corrector stage, f_o is averaged in time to recalculate the coefficients.

To illustrate the process of 2-D transport we consider a planar, fully ionized plasma of $Z = 4$ with an initial temperature of 250 eV. The ion background is kept fixed throughout the simulation with an exponential ramp of 25 μm, as shown in Fig. 36.21. A 0.35-μm laser is propagated along the positive z direction and is absorbed via a 1-D ray-trace package, as used in the hydrocode *LILAC*,[15] with a full reflection at the critical surface. The intensity of the beam is modulated in the x direction by $I = I_o[1 + \epsilon\cos(2\pi x/\lambda)]$ where $I_o = 5 \times 10^{14}$ W/cm^2 at all times.

Figure 36.21 shows the density, temperature, and absorption profiles of a 1-D simulation at 120 ps, using SPARK and a fluid code with (a) $f = \infty$ (i.e., no flux limit) and (b) $f = 0.2$. As expected, for UV light at moderate irradiances, the agreement between *FP* and *SH* calculations is very good, and the mild flux inhibition is fairly well modeled by $f = 0.2$, in agreement with Ref. 6.

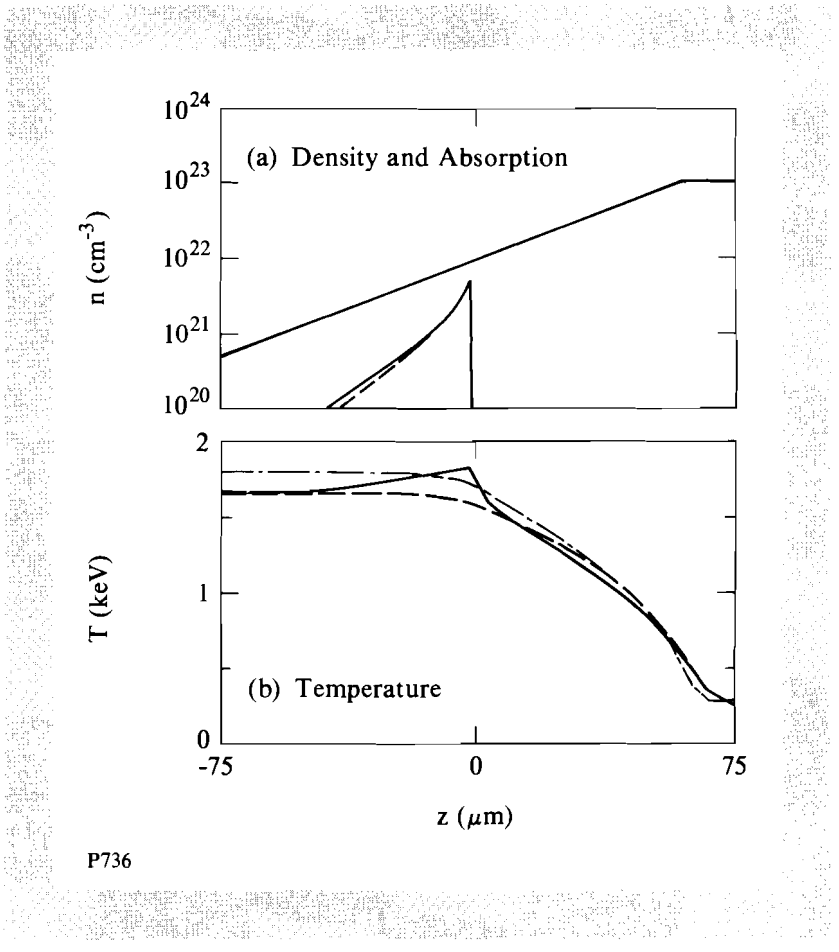

Fig. 36.21
(a) Density and energy deposition (in relative units), (b) temperature profiles for 0.35-μm irradiation at 5×10^{14} W/cm^2 after 120 ps. Solid curves refer to *FP* results; dashed and dash-dotted curves refer to *SH* results with $f = \infty$ and $f = 0.2$, respectively.

The result of nonuniform illumination is shown in Fig. 36.22 for $\epsilon = 1$ and $\lambda = 150$ μm, where the comparison is made with fluid results under no flux limitation. Here, we used (30 × 30) cells in the x-z plane and obtained a maximum charge separation of 5×10^{-5} and an energy conservation error of 6×10^{-3} for a time step of 0.1 ps. As observed from the isotherms, the smoothing predicted by the *FP* solution is less than predicted by the *SH* solution, though the average temperature $<T>$ follows the 1-D result of Fig. 36.21 very closely. This effect is highlighted in Fig. 36.23, where we plot

$$\sigma_{\text{rms}} = \{ [\int dx (T - <T>)^2] / \int dx \}^{1/2} / <T>$$

as a function of z. The peaked structure of σ_{rms} at high density is essentially an artifact of the locally sharp temperature gradients in z. Paradoxically, the simulation predicts $|q_x| < |q_z|$ and $|q_x| << fq_{fs}$ (apart from the very-low-density corona), which is normally taken to

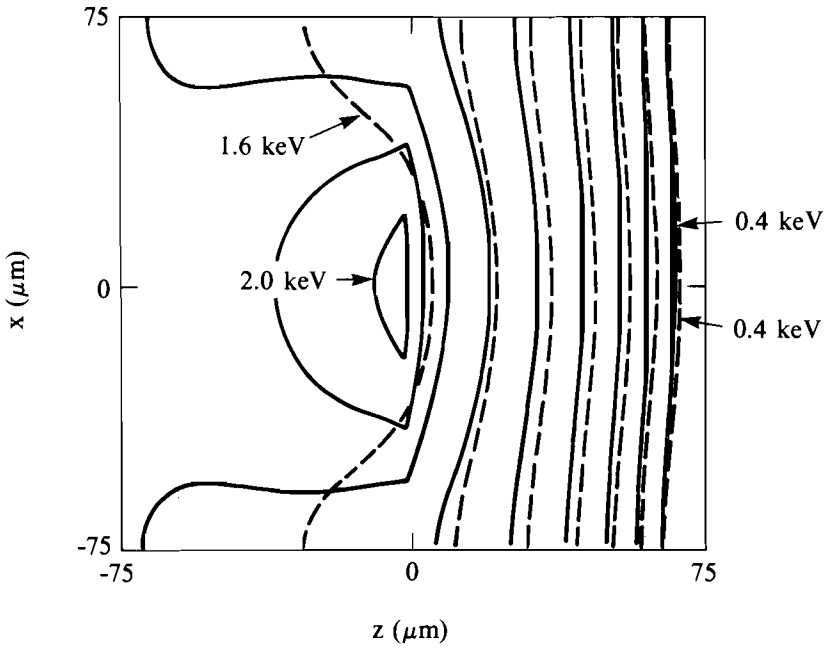

Fig. 36.22
Isotherms for nonuniform laser irradiation in steps of 0.2 keV (as in Fig. 36.21).

imply that the transverse heat transfer is close to classical. However, as has been previously shown by Bell[16] in the context of 1-D thermal transport in ion waves, the relevant criterion for nonlocal effects to be significant is that the mean free path of the heat-carrying electrons ($\approx 80\lambda_{mfp}$) is greater than the relevant spatial scale length ℓ ($= \lambda/2\pi$), irrespective of the magnitude of the heat flux. This is demonstrated quantitatively in Fig. 36.24 where we plot the ratio of *FP* to *SH* σ_{rms} as a function of ℓ/λ_{mfp}, calculated at the critical surface. The observed reduction in smoothing by the nonlocal transport is a direct consequence of heat-flux inhibition and is independent of ϵ (for $\epsilon \leq 1$). Similar results have also been obtained for different laser wavelengths and irradiances.[13] It must be noted, however, that although $(\sigma_{\text{rms}})_{FP} >> (\sigma_{\text{rms}})_{SH}$ for $\ell << \lambda_{mfp}$, both models predict that $\sigma_{\text{rms}} \rightarrow 0$ in the same limit, as seen on Fig. 36.24.

The effect of flux limiting the *SH* heat flow in 2-D is shown in Fig. 36.23 for $f = 0.2$. The relatively small improvement in the results is not surprising since the flux limitation is only weakly dependent on the lateral heat flow, which is well below fq_f. Moreover, the increased coronal temperature arising from the axial flux inhibition (see Fig. 36.21) has a tendency to increase the thermal conductivity coefficient and, hence, the amount of smoothing.

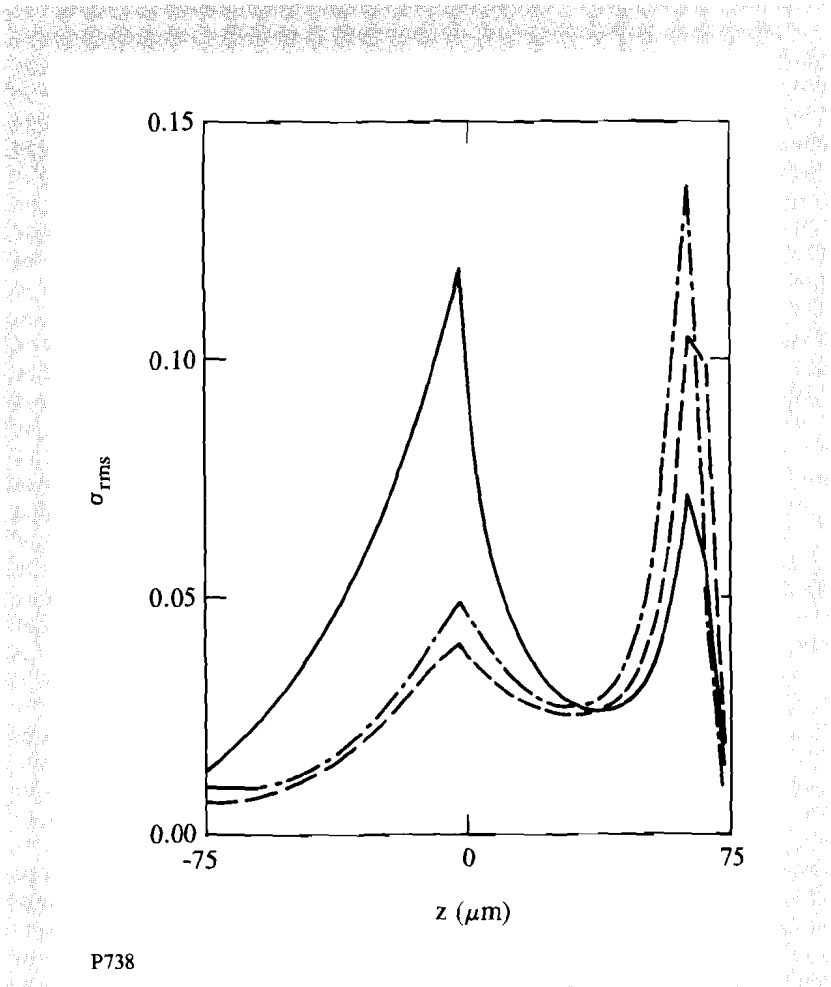

Fig. 36.23
Plot of σ_{rms} as a function of z (as in Fig. 36.21).

In summary we have shown that even when 1-D transport in laser plasmas is well described by fluid equations the same is not necessarily true in 2-D. Particularly, when there are small-scale ($\lesssim 80\lambda_{mfp}$) temperature modulations in the plasma, the thermal smoothing becomes less effective as a result of the nonlocal nature of the electron transport. This reduced smoothing, which is not adequately treated by a simple flux-limited diffusion theory, may have important implications to the process of thermal self-focusing and ultimately to the estimation of ablation pressure uniformity. In order to adequately assess these effects, SPARK has been recently extended to include the hydrodynamic response of the plasma, as well as the refraction and diffraction of the laser beam in the corona.

ACKNOWLEDGMENT

This work originated from a collaboration with Dr. A. R. Bell, supported by the Science and Engineering Research Council, United Kingdom. Its completion was supported by the U.S. Department of Energy Office of Inertial Fusion under agreement No. DE-FC08-85DP40200 and by the Laser Fusion Feasibility Project at the Laboratory for Laser Energetics, which has the following sponsors: Empire State Electric Energy Research Corporation, New York State Energy Research and Development Authority, Ontario Hydro, and the University of Rochester. Such support does not imply endorsement of the content by any of the above parties.

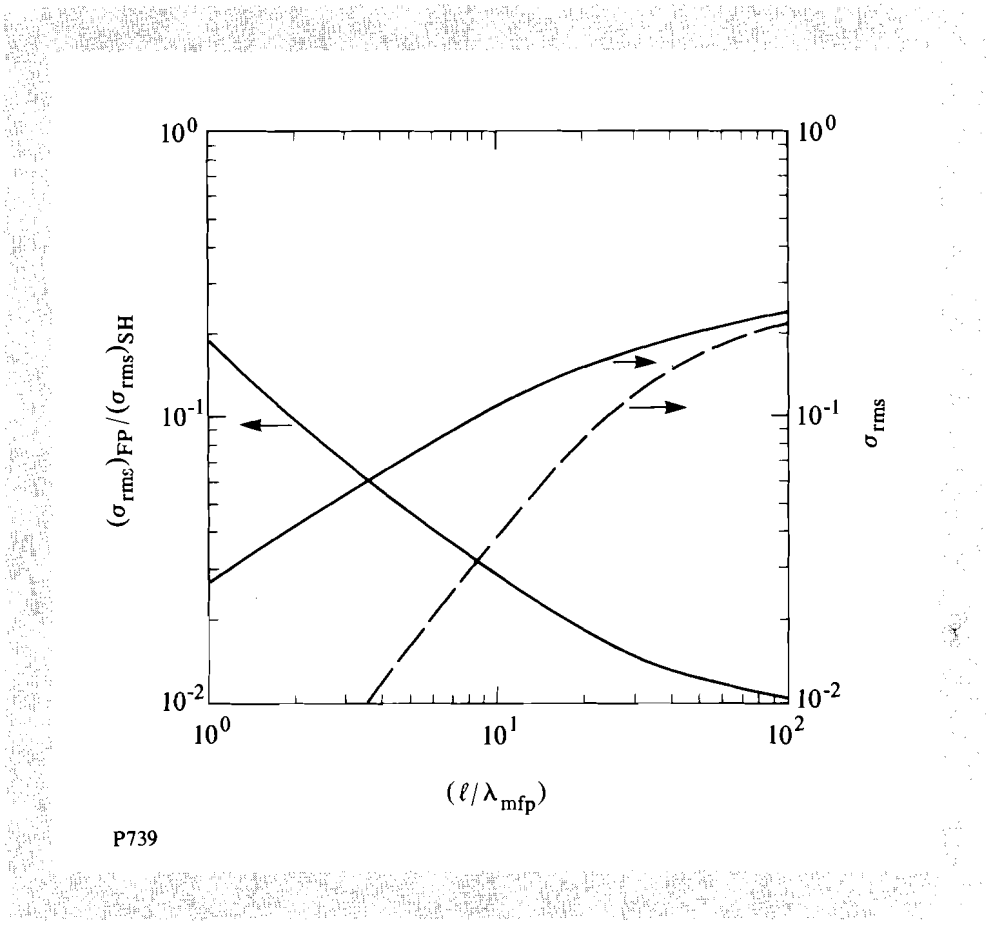

Fig. 36.24
Plots of $(\sigma_{rms})_{FP}$, $(\sigma_{rms})_{SH}$, and $(\sigma_{rms})_{FP}/(\sigma_{rms})_{SH}$ as functions of ℓ/λ_{mfp}, calculated at the critical surface (as in Fig. 36.21).

REFERENCES

1. A. R. Bell, R. G. Evans, and D. J. Nicholas, *Phys. Rev. Lett.* **46**, 243 (1981).

2. J. P. Matte and J. Virmont, *Phys. Rev. Lett.* **49**, 1936 (1982); J. R. Albritton, *ibid.* **50**, 2078 (1983); J. P. Matte, T. W. Johnston, J. Delettrez, and R. L. McCrory, *ibid.* **53**, 1461 (1984); A. R. Bell, *Phys. Fluids* **28**, 2007 (1985); T. H. Kho and M. G. Haines, *ibid.* **29**, 2665 (1986); J. Delettrez, *Can. J. Phys.* **64**, 932 (1986).

3. L. Spitzer and R. Härm, *Phys. Rev.* **89**, 977 (1953).

4. R. C. Malone, R. L. McCrory, and R. L. Morse, *Phys. Rev. Lett.* **34**, 721 (1975).

5. M. Strauss, G. Hazak, D. Shvarts, and R. S. Craxton, *Phys. Rev. A* **30**, 2627 (1984); R. S. Craxton and R. L. McCrory, *J. Appl. Phys.* **56**, 108 (1984).

6. P. A. Holstein, J. Delettrez, S. Skupsky, and J. P. Matte, *J. Appl. Phys.* **60**, 2296 (1986).

7. E. M. Epperlein, G. J. Rickard, and A. R. Bell, Laboratory for Laser Energetics, Internal Report 191, July 1988 (submitted to *Computer Physics Communications*).

8. M. H. Emery, J. H. Orens, J. H. Gardner, and J. P. Boris, *Phys. Rev. Lett.* **48**, 253 (1982); R. G. Evans, *Lasers & Part. Beams* **3**, 273 (1985); R. D. Jones *et al.*, *Phys. Fluids* **31**, 1249 (1988).

9. I. P. Shkarofsky, T. W. Johnston, and M. A. Bachynsky, *The Particle Kinetics of Plasmas* (Addison-Wesley, London, 1966).

10. A. B. Langdon, *Phys. Rev. Lett.* **44**, 575 (1980).

11. J. S. Chang and G. Cooper, *J. Comput. Phys.* **6**, 1 (1970).

12. R. J. Mason, *J. Comput. Phys.* **41**, 233 (1981).

13. E. M. Epperlein, 29th APS, Nov. 1987, San Diego, CA.

14. J. Douglas, *Numer. Math.* **4**, 41 (1962).

15. J. Delettrez (private communication); E. B. Goldman, Laboratory for Laser Energetics, Internal Report 16 (February 1973).

16. A. R. Bell, *Phys. Fluids* **26**, 279 (1983).

Section 2
ADVANCED TECHNOLOGY DEVELOPMENTS

2.A Multiphoton Ionization Experiments

In recent years, a great deal of progress has been made in the study of atomic and molecular matter under the influence of high-intensity radiation. Multiphoton ionization (MPI) studies, in particular, have been greatly advanced in several respects. Multiple-electron ionization of different atomic species has been reported with laser intensities up to $I \approx 10^{17}$ W/cm^2 with pulses lengths from 22 fs to 10–100 ns with wavelengths from 193 nm to 10.6 μm.[1] Nine times ionization of the commonly used atomic target xenon has been reported with both Nd:YLF (1.053 μm) and excimer (248-nm) lasers.

At LLE, we are studying MPI in noble gases at the highest intensities available in the 1-μm-wavelength range. We are using the so-called T^3 (table-top terawatt) laser system,[2] which operates on the principle of chirped pulse amplification (CPA) and produces up to several hundred millijoules in 1-ps pulses at a wavelength of 1.053 μm. We have observed charge states in xenon up to and including Xe^{12+} with intensities of 5×10^{16} W/cm^2 using the T^3 fundamental frequency. Xe^{8+} has been observed at 3×10^{16} W/cm^2 using frequency-doubled, 0.527-μm laser light.

Multiphoton Ionization Experiments

An atom, ion, or molecule can be ionized by the absorption of N or more photons where $N\hbar\omega$ equals the ionization potential

$$N\hbar\omega + A^{+i} \rightarrow A^{+(i+1)} + e^- \qquad (1)$$

Many authors have observed highly charged ion states produced by high-intensity laser pulses. For example, L'Huillier *et al.*[3] observed Ar^{3+}, Kr^{4+}, and Xe^{+4} ions with 50-ps, 1.06-μm, 10^{14} W/cm^2 laser pulses and Perry *et al.*[4] observed Ar^{4+}, Kr^{5+}, and Xe^{+6} ions with 1- to 2-ps, 0.58-μm, 10^{15} W/cm^2 laser pulses. Luk *et al.*[5] observed Ne^{2+}, Ar^{6+}, Kr^{6+}, and Xe^{8+} with a 193-nm ArF laser with a pulse length of 5 ps and peak intensities of 10^{17} W/cm^2. Recently, Rhodes[6] reported He^{2+}, Ne^{4+}, Ar^{8+}, Kr^{8+}, and Xe^{9+}, using a KrF laser at 248 nm, with a pulse length of 0.5 ps and intensities of roughly 10^{16} W/cm^2.

We are carrying out multiphoton ionization experiments using the T^3 laser at 1.053-μm wavelength with an 1-ps pulse duration and intensities up to 5×10^{16} W/cm^2 using *f*/4 optics. Experiments were also performed up to 3×10^{16} W/cm^2 with the second harmonic of the laser wavelength at 0.527 μm.

The laser is focused into a vacuum tank, which has a base pressure of 1×10^{-8} *T* and is typically filled to 1×10^{-5} *T* of a noble gas. The ions are detected by applying a bias voltage across the focal region and using a time-of-flight technique to obtain energy resolution. The resolution of the time-of-flight spectrometer (TOF) is sufficient to identify Xe^{13+}. The ions are detected with a dual microchannel plate with a gain of 10^6, and the spectra were recorded using a digitizing oscilloscope. An example of the relative number of argon ions detected versus laser intensity is shown in Fig. 36.25. A complete spectrum, such as this, can be obtained in approximately 3 h of run time.

We have routinely detected Ne^{5+}, Ar^{8+}, Kr^{8+}, and Xe^{9+} ions at the highest intensities. The production of each of these ions requires a last-step ionization potential of 126 eV, 143 eV, 123 eV, and 202 eV, respectively. The production of the next highest charge states Ar^{9+}, Kr^{9+}, and Xe^{10+} require ionization potentials of 422, 231, and 233 eV, respectively, whereas the production of Ne^{6+} requires an ionization potential of 156 eV. The Ar, Kr, and Xe charge states achieved are consistent with the statement that the ionization state achieved depends primarily on the ionization potentials of the atoms. An intensity of 5×10^{16} W/cm^2 appears to be sufficient to ionize atoms or ions with ionization potentials of $\sim$200 eV. This is shown in Fig. 36.26 for argon and krypton, where the appearance intensity, corresponding to the production of $\sim$40 ions of a particular charge state, or 1/250 of the number of ions at saturation of the first state, is plotted versus the ionization potential of that charge state. This figure is similar to one shown by Perry *et al.*[4] and suggests that ionization is independent of the atomic structure. It should be noted that a smooth curve of appearance intensity can also be drawn versus the sum of the ionization potentials of that particular charge state suggesting that such a plot will not discriminate between sequential and direct ionization.

Comparing our results with those of L'Huillier *et al.*[3] at 1.064 μm, we find that our appearance intensities are almost an order of magnitude larger for Ar, Kr, and Xe, whereas they are a factor of 2 larger for He. Chin *et al.*[7] showed that there can be changes in the

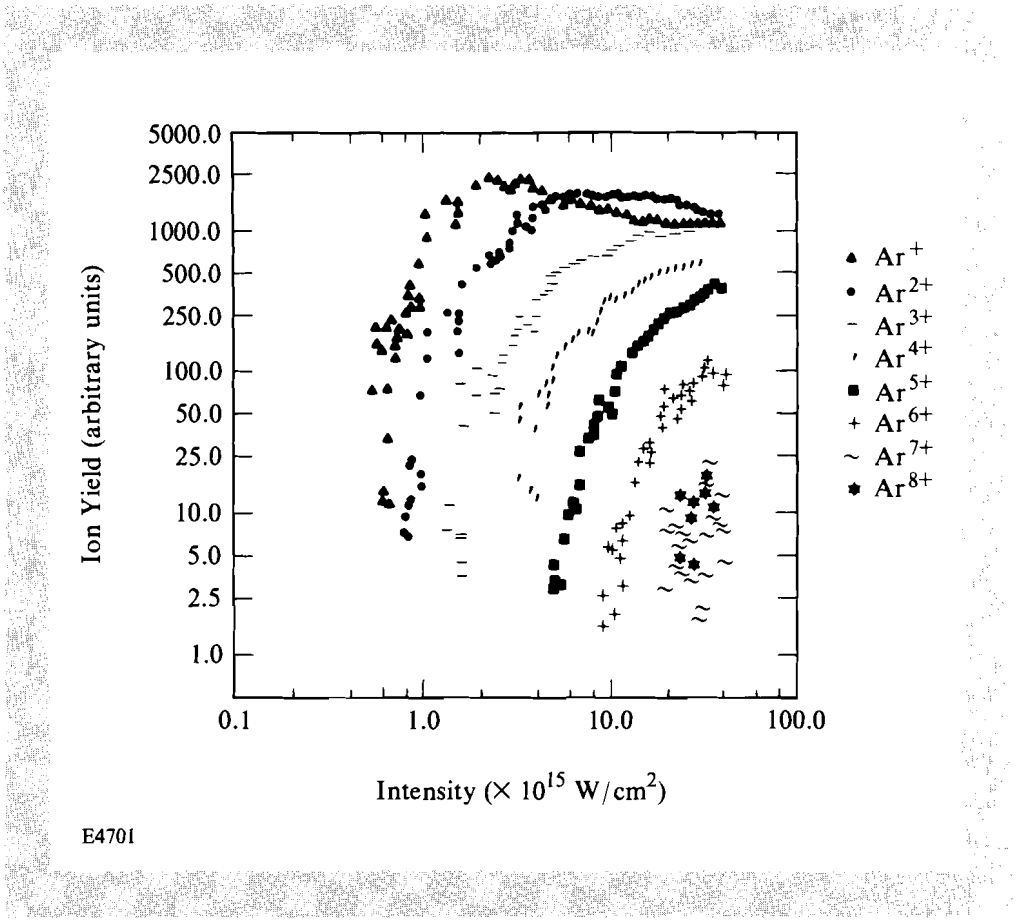

Fig. 36.25
Relative argon ion yield versus 1-μm laser intensity. The pulse width is 1 ps.

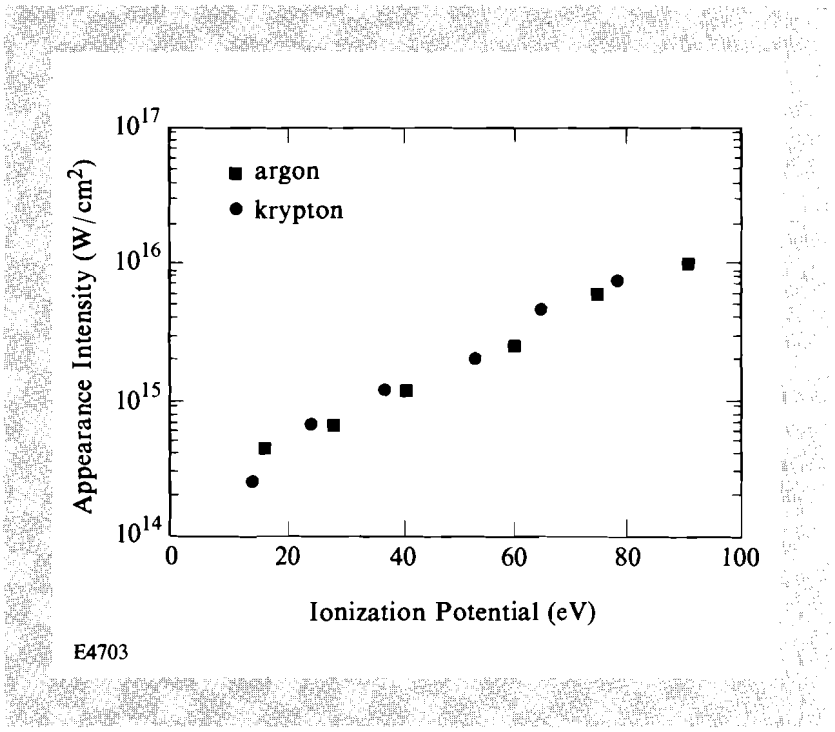

Fig. 36.26
Appearance intensity of various argon and krypton charge states versus the ionization potential of the state.

appearance intensity due to pulse-length changes; thus, we expect to find different results for L'Huillier *et al.*,[3] who worked with a 50-ps bandwidth-limited laser pulse.

While the ionization of Ar, Kr, and Xe appears to occur independently of the details of the atomic structure, Ne behaves differently. Based on the charge states achieved in the heavier elements, Ne^{6+} and perhaps Ne^{7+} (ionization potential = 207 eV) should have been observed routinely. Thus, there appears to be a significant difference between the multiphoton ionization in neon compared with the three heavier elements.

On occasional shots, Xe^{12+} was observed. The ionization potential from $Xe^{11+} \rightarrow Xe^{12+}$ is 294 eV and according to Fig. 36.26, this probably requires an intensity of 10^{17} W/cm^2, which may occur due to hot spots in the beam. The TOF spectrum showing Xe^{12+} is shown in Fig. 36.27. The observed Xe^{12+} spectra corresponds to ~10 ions. The identification is accurate to within about 3% due to space charge effects in the detected ions. We have also observed Ne^{6+} on occasional shots.

A preliminary experiment was carried out to test the effects of bandwidth versus pulse width. The xenon ion yields were compared for a 1-ps compressed pulse and a 200-ps uncompressed pulse. These two pulses have the same bandwidth and were found to give the same ion yield at the same intensity.

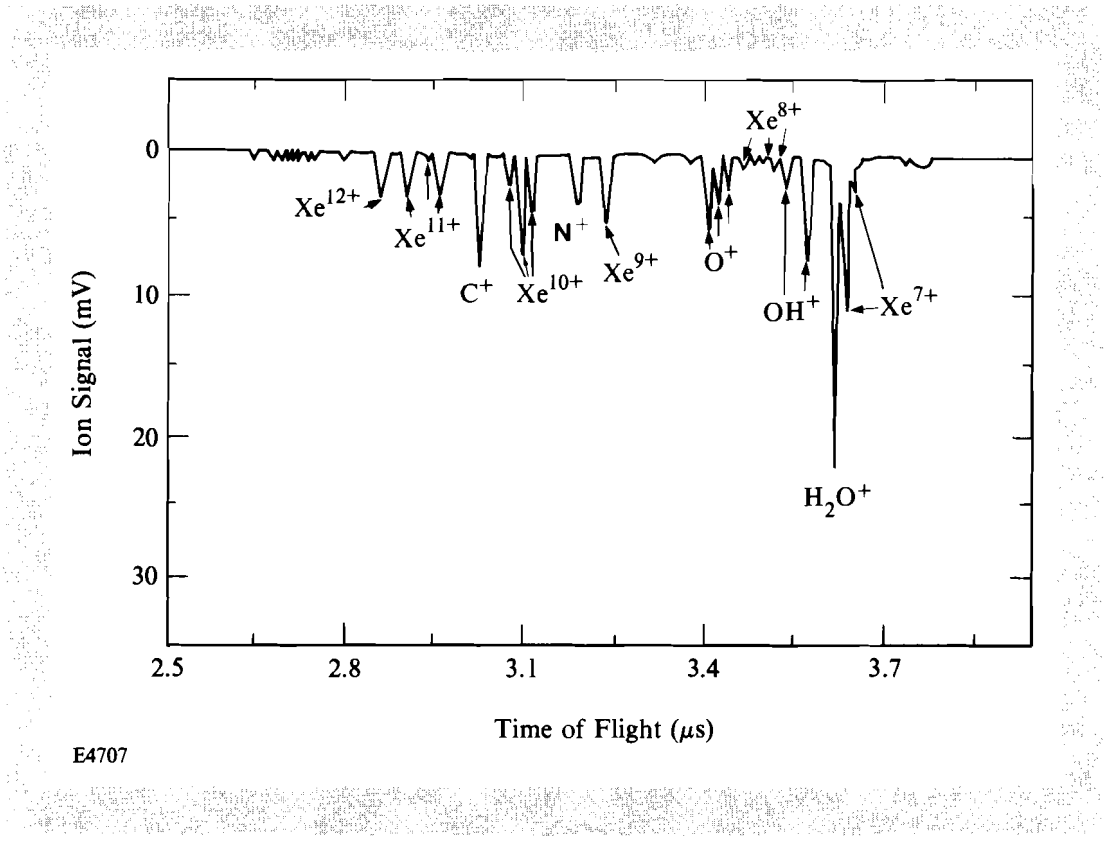

Fig. 36.27
Time-of-flight spectrum of multiphoton ionization of xenon showing Xe^{12+}.

Because of the relatively efficient frequency doubling of the laser light we were able to compare MPI at two different wavelengths. The qualitative results are that at low intensities it is easier to ionize the ions with the shorter-wavelength light, which is consistent with perturbation theory. At the highest intensities it appears that it is easier to ionize the ions with the longer-wavelength light. This is consistent with an increased importance of the pondermotive potential in the laser focus.

Summary

At LLE, we have begun multiphoton ionization experiments using the T^3 laser. This laser is currently the highest-intensity laser operating at 1-μm wavelength, with peak intensities observed up to 5×10^{16} W/cm^2. We have observed charge states up to 12 times ionized xenon with the fundamental frequency, and 8 times ionized xenon with frequency-doubled light at intensities of 3×10^{16} W/cm^2. Preliminary experiments suggest that at the highest intensities, it is easier to ionize the ions with the longer-wavelength light. We are continuing these experiments with emphasis on the effects of pulse width and bandwidth on the ionization process, and a continued comparison of the effects of different wavelengths on the process.

ACKNOWLEDGMENT

This work was supported by the National Science Foundation, the Air Force Office of Scientific Research, the Office of Naval Research, the Department of Energy Office of Inertial Fusion under agreement No. DE-FC08-85DP40200 and by the Laser Fusion Feasibility Project at the Laboratory for Laser Energetics, which has the following sponsors: Empire State Electric Energy Research Corporation, New York State Energy Research and Development Authority, Ontario Hydro, and the University of Rochester. Such support does not imply endorsement of the content by any of the above parties.

REFERENCES

1. The most recent overviews of this work can be found in M. Crance, *Phys. Rep.* **144**, 117 (1987); in C. K. Rhodes, *Phys. Scr.* **T17**, 193 (1987); and in *Multiphoton Processes*, edited by S. J. Smith and P. L. Knight (Cambridge University Press, Cambridge, England, 1988).
2. P. Maine, D. Strickland, P. Bado, M. Pessot, and G. Mourou, *IEEE J. Quantum Electron.* **24**, 398 (1988).
3. A. L'Huillier, L. A. Lompré, G. Mainfray, and C. Manus, *J. Phys. B.* **16**, 1363 (1983).
4. M. D. Perry, A. Szoke, O. L. Landen, and E. M. Campbell, *Phys. Rev. Lett.* **60**, 1270 (1988).
5. T. S. Luk, U. Johann, H. Egger, H. Pummer, and C. K. Rhodes, *Phys. Rev. A* **32**, 214 (1985).
6. C. K. Rhodes (see Ref. 1).
7. S. L. Chin, C. Rolland, P. B. Corkum, and P. Kelley, *Phys. Rev. Lett.* **61**, 153 (1988).

Section 3
NATIONAL LASER USERS FACILITY NEWS

During the fourth quarter of FY88 a great deal of time and effort went into supporting the experiments of **J. Apruseze**, **U. Feldman**, and **H. Griem**. All of these experiments used the line-focus geometry on OMEGA. The operations crew did an excellent job with laser pointing and target alignment.

J. Apruseze from NRL continued with his investigation of "hot-electron" pumping of neon-like ions. This experiment required OMEGA in line focus and GDL as ALPHA in line focus. X-ray and XUV spectra were taken for silver targets with two different irradiation intensities with and without ALPHA. There was some concern that the line-focus geometry did not have sufficient intensity to heat the plasma to the neon-like ionization state. Preliminary analysis of the 3-m grazing incidence spectrograph data and the Burkhalter crystal spectrograph data indicate that the plasma did not get hot enough to create neon-like ions. **P. Burkhalter** and **J. Seely** are analyzing the data to determine the distribution of ionization states in the silver plasma. With no neon-like silver present, it was impossible to see the effect of collisional pumping with the hot electrons created by the ALPHA beam when it irradiated the target.

H. Griem's experiment was conducted by **J. Moreno**. This experiment was to study the radiative cooling of a linear plasma by high-Z elements. Targets of Al and Au layers were irradiated with the OMEGA laser and x-ray and XUV spectra were recorded with the 3-m

grazing incidence spectrograph and SPEAXS. J. Moreno is analyzing this data at the University of Maryland.

U. Feldman from NRL has recorded XUV spectra from several targets irradiated with line-focused beams. Spectra were recorded both axially and radially with respect to the plasma cylinder. The axial spectra were recorded with the 3-m grazing incidence spectrograph and radial spectra were recorded with a NRL 1-m grazing incidence spectrograph. Very narrow XUV line radiation was recorded on the 3-m spectrograph. The plasma predominantly expands in the radial direction. Therefore, the doppler shift in the line energy was not present. J. Seely is continuing to analyze the data and is quite pleased with its quality.

The contract office of the DOE has been changed. From now on, all NLUF contracts will be handled by the San Francisco office instead of the Las Vegas office. The contact at the San Francisco office is **Dennis Neely**. All proposals for FY90 are due at DOE, San Francisco, on the 15 December 1988. This is a change from previous years when proposals were sent to the University of Rochester Laboratory for Laser Energetics.

ACKNOWLEDGMENT

This work was supported by the U.S. Department of Energy Office of Inertial Fusion under agreement No. DE-FC08-85DP40200.

Section 4
LASER SYSTEM REPORT

4.A GDL Facility Report

The glass development laser (GDL) was used by three target interaction groups during this quarter. Experiments were conducted in the Beta target irradiation facility and concentrated on x-ray laser studies, x-ray lithography, and the transmission of light through multilayered targets. The x-ray laser experiments were aimed at observing gain in collisionally pumped neon-like nickel and germanium. The x-ray lithography experiment measured the silicon content of corn, which may serve as a new source of ultra-pure silicon. The third campaign supports OMEGA experiments in an attempt to understand the temporal behavior of multilayered targets. In addition to the target interaction experiments, several shots were used to calibrate a new Kodak film.

A summary of GDL operations this quarter follows:

Beamline Test, Calibration, Tuning, and Laser Alignment Shots	348
Test Shots	
X-Ray Laser	105
X-Ray Lithography	45
Multilayer Experiments	166
TOTAL	664

4.B OMEGA Facility Report

The OMEGA laser and target systems have been active in target shooting and laser uniformity experiments during this quarter. X-ray laser campaigns dominated the target interaction programs, and several new approaches to laser uniformity were explored.

For the x-ray laser target shots, OMEGA was configured in an eight-beamline focus geometry. Cylindrical lenses were added to the final focusing elements, bringing each beam to a 100-μm $\times$ 1500-μm spot. Several irradiation geometries were delivered to a variety of targets, including a superimposed, short-pulse IR beam from the GDL facility, synchronized to the peak of the OMEGA beams. After the x-ray laser experiments were completed, the system was reconfigured to 24-beam spherical geometry. Target and laser uniformity test shots filled out the remainder of this reporting period, with laser uniformity improvements taking top priority. The beam analysis table (BAT) was used to interferometrically measure the wave front of each of the 24 beams. The BAT can be positioned in any beam within 15 min., so pulsed and cw phase information can be easily obtained. Based on the data, adjustments were made to the collimation of the driver line prior to the 24-way split, using defocus at the input of the system to compensate for the spherical aberration of beamline components.

In September, a power balance campaign that uses both energy and pulse shape information to equalize the temporal history of the beams was begun on OMEGA. Two new techniques were developed to measure the pulse width: a high-speed photodiode coupled to a 6-GHz oscilloscope; and a multibeam system that uses optical fibers to couple four beams simultaneously into a streak camera.

A summary of OMEGA operations for this quarter follows:

Target Shots	
Line-Focus	86
Spherical	86
Driver Line Shot and Tests	73
Laser Test and Alignment Shots	137
TOTAL	382

ACKNOWLEDGMENT

This work was supported by the U. S. Department of Energy Office of Inertial Fusion under agreement No. DE-FC08-85DP40200 and by the Laser Fusion Feasibility Project at the Laboratory for Laser Energetics, which has the following sponsors: Empire State Electric Energy Research Corporation, New York State Energy Research and Development Authority, Ontario Hydro, and the University of Rochester. Such support does not imply endorsement of the content by any of the above parties.

PUBLICATIONS AND CONFERENCE PRESENTATIONS

Publications

W. Watson, "Vacuum-Assisted Contaminated-Particulate Removal," *J. Vac. Sci. Technol. A* **6**, 2568–2570 (1988).

R. L. McCrory, J. M. Soures, C. P. Verdon, F. J. Marshall, S. A. Letzring, S. Skupsky, T. J. Kessler, R. L. Kremens, J. P. Knauer, H. Kim, J. Delettrez, R. L. Keck, and D. K. Bradley, "Laser-Driven Implosion of Thermonuclear Fuel to 20 to 40 g cm^{-3}," *Nature* **335**, 225–230 (1988).

S. D. Jacobs, K. A. Cerqua, K. L. Marshall, A. Schmid, M. J. Guardalben, and K. J. Skerrett, "Liquid-Crystal Laser Optics: Design, Fabrication, and Performance," *J. Opt. Soc. Am. B* **5**, 1962–1979 (1988).

S. D. Jacobs, K. A. Cerqua, K. L. Marshall, A. Schmid, M. J. Guardalben, and K. J. Skerrett, "Liquid Crystal Optics for Laser Systems," *Laser Optics for Intracavity and Extracavity Applications* (SPIE, Bellingham, WA, 1988), Vol. 895, pp. 120–151.

K. L. Marshall, A. W. Schmid, D. J. Smith, A. A. Bevin, M. J. Guardalben, and S. D. Jacobs, "Performance of Protective Polymeric Coatings for Nonlinear Optical Materials," *J. Appl. Phys.* **64**, 2279–2285 (1988).

P. C. Cheng, H. G. Kim, D. M. Shinozaki, K. H. Tan, and M. D. Wittman, "X-Ray Microscopy—Its Application to Biological Sciences," *X-Ray Microscopy II, Proceedings of the International Symposium 1987*, edited by D. Sayre, M. Howells, J. Kirz, and

H. Rarback (Springer-Verlag, Berlin, Heidelberg, New York, London, Paris, Tokyo, 1988), pp. 356–364.

R. Q. Gram, C. K. Immesoete, H. Kim, and L. Forsley, "Bounce-Coated Ablation Layers on Fusion Targets," *J. Vac. Sci. Technol. A* **6**, 2998–3001 (1988).

S. Goldsmith, J. C. Moreno, H. R. Griem, L. Cohen, and M. C. Richardson, "Relative Ion Expansion Velocity in Laser-Produced Plasmas," *J. Appl. Phys.* **64**, 581–585 (1988).

W. E. Behring, J. H. Underwood, C. M. Brown, U. Feldman, J. F. Seely, F. J. Marshall, and M. C. Richardson, "Grazing Incidence Technique to Obtain Spatially Resolved Spectra from Laser Heated Plasmas," *Appl. Opt.* **27**, 2762–2767 (1988).

J. F. Whitaker, G. A. Mourou, T. C. L. G. Sollner, and W. D. Goodhue, "Picosecond Switching Time Measurement of a Resonant Tunneling Diode," *Appl. Phys. Lett.* **53**, 385–387 (1988).

C. A. Amsden, S. E. Gilman, S. D. Jacobs, and J. S. Torok, "Measurement of the Thermal Conductivity of Dielectric Thin Solid Films with a Thermal Comparator," *The Optical Interference Coatings 1988 Technical Digest* **6**, 78–81 (1988).

S. H. Chen and Y. F. Maa, "A Reexamination of the Synthesis of Liquid Crystalline Side-Chain Polyacrylates via Liquid-Liquid Phase Transfer Catalysis," *Macromolecules* **21**, 904–907 (April 1988).

S. H. Chen and Y. F. Maa, "Preparation of Liquid Crystalline Side-Chain Polyacrylate by Chemically Modifying Poly(sodium acrylate) in Hexamethylphosphoramide," *Macromolecules* **21**, 2697–2699 (1988).

C. Bamber, W. Donaldson, T. Juhasz, L. Kingsley, and A. C. Melissinos, "Radial Compression of Picosecond Electrical Pulses," *Particle Accelerators* **23**, 255–263 (1988).

Forthcoming Publications

A. Simon, S. Radin, and R. W. Short, "Long-Time Simulation of the Single-Mode Bump-on-Tail Instability," to be published in *Physics of Fluids.*

J. S. Coe, P. Maine, and P. Bado, "Regenerative Amplification of Picosecond Pulses in Nd:YLF: Effect of Gain Narrowing and Gain Saturation," to be published in the *Journal of the Optical Society of America B.*

S. H. Batha, R. Bahr, L. M. Goldman, W. Seka, and A. Simon, "Observations of Enhanced Thomson Scattering," to be published in *Physics of Fluids.*

J. C. Lee, A. Schmid, and S. D. Jacobs, "Effects of Anchoring Under Intense Optical Fields in a Cholesteric Liquid Crystal," to be published in *Molecular Crystals and Liquid Crystals.*

R. Epstein, "The Design and Optimization of Recombination XUV Lasers," to be published in *Physics of Fluids.*

E. M. Epperlein, G. J. Rickard, and A. R. Bell, "A Code for the Solution of the Vlasov-Fokker-Planck Equation in 1-D or 2-D," to be published in *Computer Physics Communications.*

R. L. McCrory, "Computer Modelling and Simulation in ICF," to be published in *Il Nouvo Cimento.*

W. R. Donaldson, "Radial Line Structure Experiments," to be published in the *Proceedings of the 4th Workshop: Pulse Power Techniques for Future Accelerators*, Erice, Sicily, 3-10 March 1988.

J. C. Lee, J. H. Kelly, D. L. Smith, and S. D. Jacobs, "Gain Squaring in a Cr:Nd:GSGG Active Mirror Amplifier Using a Cholesteric Liquid Crystal Mirror," to be published in the *IEEE Journal of Quantum Electronics.*

M. C. Richardson, D. K. Bradley, P. A. Jaanimagi, J. Delettrez, R. Epstein, C. F. Hooper, R. C. Mancini, and D. Kilcrease, "X-Ray Diagnosis of High-Density Compression of Ar-Filled Polymer Shell Targets," to be published in the *Review of Scientific Instruments.*

A. Simon and R. W. Short, "Alternative Analysis of CO_2-Laser-Produced Plasma Waves," to be published in *Physics of Fluids.*

P. Maine and G. Mourou, "Amplification of 1 ns Pulses in Nd:Glass Followed by Compression to 1 ps," to be published in *Optics Letters.*

P. C. Cheng, S. P. Newberry, H. Kim, and M. D. Wittman, "X-Ray Contact Microradiography and Shadow Projection X-Ray Microscopy," to be published in the *European Journal of Cell Biology.*

R. L. McCrory, J. M. Soures, C. Verdon, M. Richardson, P. Audebert, D. Bradley, J. Delettrez, L. Goldman, R. Hutchison, S. Jacobs, P. Jaanimagi, R. Keck, H. Kim, T. Kessler, J. Knauer, R. Kremens, S. Letzring, F. Marshall, P. McKenty, W. Seka, S. Skupsky, and B. Yaakobi, "High-Density Laser-Fusion Experiments at the Laboratory for Laser Energetics," to be published in the *Proceedings of the 8th International Workshop on Laser Interaction and Related Plasma Phenomena.*

The following papers are to be published in the *Proceedings of SPIE's 32nd International Technical Symposium on Optical and Optoelectronic Applied Science and Engineering* (SPIE, Bellingham, WA, 1988):

D. K. Bradley, P. A. Jaanimagi, J. Delettrez, C. P. Verdon, F. Marshall, J. D. Kilkenny, and P. Bell, "X-Ray Gated Images of Imploded Microballoons."

P. A. Jaanimagi, D. D. Meyerhofer, and M. C. Richardson, "Diagnosing One Picosecond Duration Ultra-High Brightness Sources."

G. Mourou, "Picosecond Electro-Optic Sampling," to be published in the *Proceedings of the High Speed Electronics Conference*, Stockholm, Sweden, August 1986.

R. L. McCrory and J. M. Soures, "Inertially Confined Fusion," to be published in *Applications of Laser Plasmas,* Chapter 7.

O. Barnouin, B. Yaakobi, J. Delettrez, R. Epstein, P. Jaanimagi, and L. M. Goldman, "Experimental and Numerical Study of Thermal Transport in 24-Beam Ultraviolet Irradiation of Spherical Targets," to be published in the *Journal of Applied Physics.*

E. M. Epperlein, G. J. Rickard, and A. R. Bell, "Two-Dimensional Nonlocal Electron Transport in Laser-Produced Plasmas," to be published in *Physical Review Letters.*

S. Krishnamurthy and S. H. Chen, "Purification of Thermotropic Liquid Crystalline Siloxane Oligimer with Supercritical Carbon Dioxide," to be published in *Makromol. Chem.*

Conference Presentations

The following presentations were made at the 6th International Conference of Ultrafast Phenomena, Kyoto, Japan, 12–15 July 1988:

J. F. Whitaker, G. A. Mourou, T. C. L. G. Sollner, and W. D. Goodhue, "Tunneling-Time Measurements of a Resonant Tunneling Diode."

G. Mourou, D. Dykaar, J. Chwalek, J. Whitaker, and T. Hsiang, "Superconducting Lines for Interconnects and Communication."

P. Maine, D. Strickland, P. Bado, and G. Mourou, "Terawatt Pulses Obtained by Chirped Pulse Amplification."

The following presentations were made at IQEC '88 XVI International Conference on Quantum Electronics, Tokyo, Japan, 18–21 July 1988:

J. F. Whitaker, G. A. Mourou, T. C. L. G. Sollner, and W. D. Goodhue, "Switching-Time Measurements of a Resonant-Tunneling Diode."

P. Maine, D. Strickland, P. Bado, M. Pessot, J. Squier, G. Mourou, and D. Harter, "Ultrahigh Peak Power Pulses from Solids Using Chirped Pulse Amplification."

H. E. Elsayed-Ali and G. A. Mourou, "Picosecond Reflection High-Energy Electron Diffraction."

J. M. Chwalek, D. R. Dykaar, J. F. Whitaker, R. Sobolewski, T. Y. Hsiang, G. Mourou, D. K. Lathrop, S. E. Russek, and R. A. Buhrman, "Propagation Characteristics of Picosecond Electrical Transients on Thin Film $YBa_2Cu_3O_{7-y}$ Transmission Lines."

J. Noh, H. Elsayed-Ali, and G. Mourou, "Transport of SiO_2 on the Picosecond and Femtosecond Time Scales," presented at the SDI/IST-Funded Research Program on Reliable Advanced Electronic Systems, Arlington, VA, 27–28 July 1988.

R. L. McCrory, "High Power Laser Systems Applications to ICF," presented at the 35th Scottish Universities Summer School in Physics, St. Andrews, Scotland, 12–20 August 1988.

The following presentations were made at SPIE's 32nd International Technical Symposium on Optical and Optoelectronic Applied Science and Engineering, San Diego, CA, 14–19 August 1988:

D. K. Bradley, P. A. Jaanimagi, J. Delettrez, C. P. Verdon, F. Marshall, J. D. Kilkenny, and P. Bell, "X-Ray Gated Images of Imploded Microballoons,"

P. A. Jaanimagi, D. D. Meyerhofer, and M. C. Richardson, "Diagnosing One Picosecond Duration Ultra-High Brightness Sources."

The following presentations were made at the 1988 Applied Superconductivity Conference, San Francisco, CA, 21–25 August 1988:

P. H. Ballentine, M. A. Fisher, A. M. Kadin, and W. R. Donaldson, "Microlithography of High-Temperature Superconducting Films: Laser Ablation versus Wet Etching."

D. R. Dykaar, R. Sobolewski, and T. Y. Hsiang, "Picosecond Switching Dynamics of a Josephson Tunnel Junction."

D. R. Dykaar, J. M. Chwalek, R. Sobolewski, J. F. Whitaker, T. Y. Hsiang, G. A. Mourou, D. K. Lathrop, S. E. Russek, and R. A. Buhrman, "Picosecond Pulse Propagation on Superconducting Transmission Lines."

R. L. Mccrory, "Computer Modeling and Simulation in ICF," presented at the International School of Plasma Physics /Inertial Confinement Fusion Course and Workshop, Varenna, Italy, 6–16 September 1988.

D. Shire, T. Jackson, P. Tasker, D. Radulescu, L. Eastman, and G. Mourou, "Characterization of Traveling-Wave MODFET's by Electro-Optic Sampling," presented at the 15th Annual International Symposium on GaAs and Related Compounds, Atlanta, GA, 11–14 September 1988.

ACKNOWLEDGMENT

The work described in this volume includes current research at the Laboratory for Laser Energetics, which is supported by Empire State Electric Energy Research Corporation, New York State Energy Research and Development Authority, Ontario Hydro, the University of Rochester, and the U.S. Department of Energy Office of Inertial Fusion under agreement No. DE-FC08-85DP40200.